geosciences

MDPI

Article

Wildfires and Monsoons: Cryptic Drivers for Highly Variable Provenance Signals within a Carboniferous Fluvial System

Béibhinn Anders [1,2,*], Shane Tyrrell [1,2,3], David Chew [3,4], Gary O'Sullivan [5], Chris Mark [5,†], John Graham [4], Eszter Badenszki [3,5] and John Murray [1,3]

1 Earth and Ocean Sciences, School of Natural Sciences, NUI Galway, University Road, H91 CF50 Galway, Ireland; shane.tyrrell@nuigalway.ie (S.T.); john.murray@nuigalway.ie (J.M.)
2 Sediment Origins Research Team (SORT), NUI Galway, University Road, H91 CF50 Galway, Ireland
3 Irish Centre for Research in Applied Geosciences (iCRAG), University College Dublin, D04 V1W8 Dublin, Ireland; CHEWD@tcd.ie (D.C.); eszter.badenszki@ucd.ie (E.B.)
4 Department of Geology, Trinity College Dublin, College Green, D02 PN40 Dublin, Ireland; JRGRAHAM@tcd.ie
5 UCD School of Earth Sciences, University College Dublin, D04 V1W8 Dublin, Ireland; gary.osullivan@ucd.ie (G.O.); chris.mark@ucd.ie (C.M.)
* Correspondence: b.anders1@nuigalway.ie
† Current affiliation: Department of Geosciences, Swedish Museum of Natural History, Svante Arrhenius väg 3, 114 18 Stockholm, Sweden.

Abstract: Sediment delivery and supply are explicitly controlled by variations in broad-scale processes such as climate, tectonics and eustasy. These in turn influence fluvial processes and hinterland evolution. A bespoke multi-proxy approach (integrating apatite and zircon U-Pb geochronology, trace elements in apatite, and Pb-in-K-feldspar provenance tools) coupled with outcrop investigation is used to constrain the temporal trends in sediment delivery to channel sandstones of the fluvio-estuarine mid-Viséan Mullaghmore Sandstone Formation, Ireland. Provenance data indicate unique detrital signatures for all sampled horizons, indicating the fluctuating nature of sediment supply to this medium-sized basin. Tectonism and/or abrupt relative sea-level fall likely caused fluvial rejuvenation, resulting in local basement sourcing of the initial fill. Older and more distal sources, such as the Nagssugtoqidian Belt of East Greenland, become more prominent in stratigraphically younger channel sandstones suggesting catchment expansion. Paleoproterozoic to Mesoproterozoic sources are most dominant, yet the detrital grain cargo varies in each channel sandstone. Proximal sources such as the Donegal Batholith and Dalradian Supergroup are variable and appear to switch on and off. These signal shifts are likely the result of channel migration and paleoclimatic fluctuation. A monsoonal climate and large-scale wildfire events (evidenced by fusain) likely contributed to modify plant cover, intensify erosion, and increase run-off and sediment delivery rates from specific areas of the hinterland.

Keywords: provenance; temporal variation; sediment supply; paleoclimate; fusain; zircon; apatite; K-feldspar

Citation: Anders, B.; Tyrrell, S.; Chew, D.; O'Sullivan, G.; Mark, C.; Graham, J.; Badenszki, E.; Murray, J. Wildfires and Monsoons: Cryptic Drivers for Highly Variable Provenance Signals within a Carboniferous Fluvial System. *Geosciences* **2022**, *12*, 20. https://doi.org/10.3390/geosciences12010020

Academic Editors: Salvatore Critelli and Jesus Martinez-Frias

Received: 19 November 2021
Accepted: 27 December 2021
Published: 4 January 2022

Publisher's Note: MDPI stays neutral with regard to jurisdictional claims in published maps and institutional affiliations.

1. Introduction

Fluvial erosion and sedimentation are dependent on many factors, including large-scale global changes such as climate [1–4], sea level changes [5–7], and tectonism [8–10], all of which may be intrinsically interlinked. Changes in climatic state may be reflected and recorded in the sedimentary record much more rapidly compared to changes in tectonic state, which can take up to 100 kyr^{-1} myr to emerge in the sedimentary archive due to the lag in the erosion and transfer subsystems, highlighting that the time between erosion and deposition is not always instantaneous [11,12].

Smaller local- to regional-scale variations, such as channel avulsion and migration [13,14], hinterland evolution and basement un-roofing [9,15,16], and episodic (catastrophic) events

such as storms, landslides or hillslope wasting [17,18], typhoons [19] or wildfires [20–23], for example, all further impact sedimentation trends. In fluvial systems affected by wildfires, discharge (water, sediment, and suspended-sediment concentrations) increases for several years post wildfire [24,25]. This sediment load increase is, furthermore, highly dependent on rainfall trends following the wildfire event [26,27]. Warrick et al. [27] investigated the effects on sediment discharge for a ~300 km^2 watershed in California, which experienced a major wildfire in August 1977, followed by an unusually wet winter. The suspended sediment yield (coarse and fine) was c.35 times higher than average in the year following the fire event. The increase in sediment yield was due to increased erosion of soils following the removal of plant cover. Vegetation plays a key role in sediment stabilization e.g., [28,29], and controlling the resultant sediment flux in fluvial systems, e.g., [30,31]. Wildfire further increases organic sediment supply to basins, which has implications for the burial of residue wildfire material that does not easily oxidize or degrade, and potential carbon sequestration [32].

The effects and processes detailed above are recorded differently in large-scale fluvial systems compared to small- to medium-scale systems where variability in sediment delivery is higher [11,33,34]. This is because small- to medium-scale systems are particularly sensitive to external impacts such as climate, channel migration, sediment storage and varying erosional processes than larger fluvial systems, which have more effective storage zones and homogenize more readily. The location and climatic zone of the fluvial system also plays a role, controlling the nature, type and extent of plant cover, with semi-arid conditions and high latitudes generally sparsely vegetated compared to tropical forests. Wet tropics have relatively high denudation rates, and arid low latitudes have lower denudation and erosion rates [35–37]. Fielding et al. [38] suggested that tropical and subtropical rivers yield a highly variable discharge, and resultant sedimentological fills can be highly heterogeneous.

Investigating temporal changes in modern rivers is important for addressing many acute problems faced by society today, such as erosion, avulsion, basin sedimentation, and flooding. An understanding of ancient fluvial systems provides a baseline for systems unaffected by anthropogenic activity. At present, over 95% of rivers are influenced by human activity [39] with dams, reservoirs, bank stabilisation and various other engineered structures affecting sediment erosion, transport and deposition, e.g., [7,40–44], with the impacts even surpassing climatic effects on fluvial systems [33]. Very few rivers today run through pristine and uncultivated natural landscapes or comprise a catchment void of anthropogenic activity, further influencing detrital sediment signatures. Peng et al. [43] assessed sediment flow in the Yellow River in China between 1950 and 2007 and observed a gradual decrease in sediment load with increasing anthropogenic influence. Assessing modern-day flow regimes, and sedimentation processes and rates in fluvial systems is of fundamental importance to better understanding their ancient fluvial counterparts. However, direct comparison of these ancient and potentially modern analogues should be made cautiously, and with a comprehensive understanding of all the variables that affect sedimentary systems and the surrounding environment over extended (geological) timescales.

A range of studies have assessed temporal variation in Quaternary and modern sediments and rivers, e.g., [6,43] and references therein, yet understanding of the long-term fluvial trends in ancient (older than Cenozoic) sedimentary records remains poor. In provenance studies from subsurface basins, it is evident that lack of 3D rock exposure and the difficulty in obtaining samples hinders the assessment of high-resolution temporal provenance variability within the fluvial systems feeding these basins [45,46].

Multi-proxy provenance studies of temporal variation in fluvial sedimentation, focussing only on channel sandstones or point bars within one discrete ancient fluvial system, are intrinsically limited. The true extent of the variability in sediment supply within depositional sequences over long timescales continues to remain unclear.

This contribution aims to assess ancient fluvial dynamics within a Carboniferous fluvio/estuarine system in order to address some of the issues identified above. To en-

able a more thorough understanding of temporal variation in ancient sediment supply, mid-Viséan channel sandstone facies units in western Ireland were sampled and analysed through application of a bespoke multi-proxy provenance approach. This included both mechanically and chemically stable (zircon), intermediate (apatite) and labile (K-feldspar) mineral phases. Assessing a range of mineral suites with differing chemical and physical properties is key to 'finding' and discerning all grain populations/sources and gaining the maximum information on the detrital components within any sedimentary system, e.g., [47,48]. This approach aims to garner high-resolution provenance data by investigating the original source-to-sink sediment pathways and examining how provenance signatures vary in each channel sandstone unit, collectively representing evolution of the system through time. Provenance analysis is key in assessing how sand supply fluctuated in depositional systems, in deciphering the principal controls on sedimentation trends, and also in determining the extent to which external factors (such as climate, episodic events such as wildfires or landslides, etc.) impact sediment supply and composition. While it is important to address these issues for paleogeographic reconstruction and reservoir/aquifer quality, these insights are also important for anticipating future fluvial trends and establishing more precisely how dramatic hinterland evolution influences river systems.

The study site is located onshore in northwest Ireland (Figure 1) and has excellent outcrop exposure of five broadly repetitive channel sandstone facies packages assigned to the mid-Viséan Mullaghmore Sandstone Formation. These clastic units were deposited relatively rapidly and experienced minimal post depositional deformation, rendering this an ideal study site.

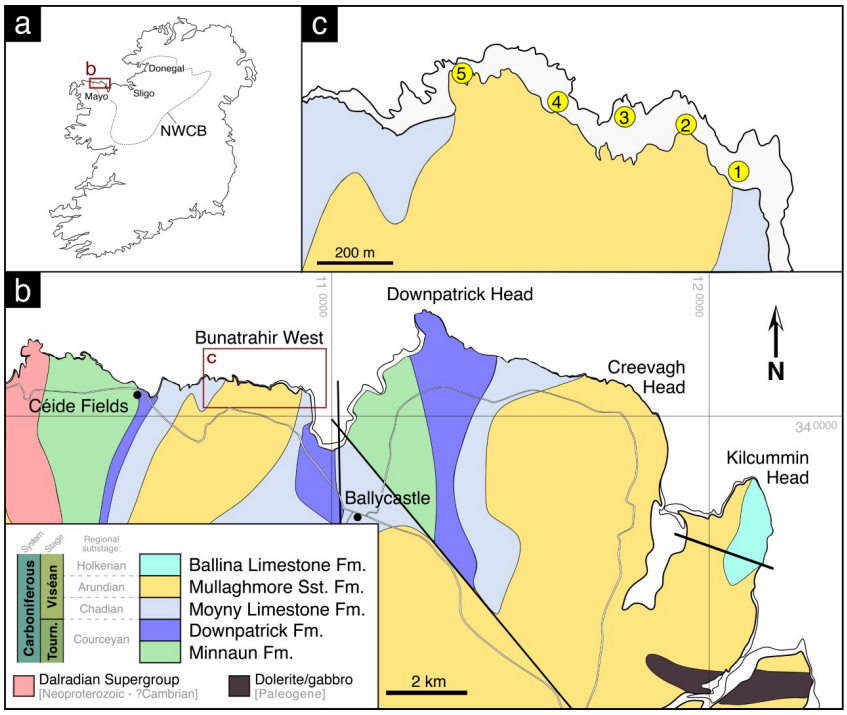

Figure 1. Geographic location and stratigraphic context of the study area. (**a**) Location of the Northwest Carboniferous Basin (NWCB) in Ireland. Inset box shows the location of geological map in b. (**b**) Geological map of North Mayo, after Graham [49]. Inset box shows location of more detailed map of study area in c. (**c**) Mullaghmore Sandstone Formation at Bunatrahir West with sample locations (yellow numbered circles). The lithostratigraphical key is applicable to the maps in b and c; it also shows the chronostratigraphic position of the Carboniferous succession in north Mayo. Placement of regional substage boundaries is quite tentative (they are dashed as a result). Tourn. = Tournaisian Stage. Dalradian Supergroup metasedimentary rocks form the geological basement in the study area.

Paleoenvironment and Geological Setting of the Mullaghmore Sandstone Formation

During the Carboniferous (Mississippian), Ireland was located just south of the paleoequator in tropical latitudes [50–52]. Carbonate production became widespread across much of northwestern Europe during the Mississippian, with terrigenous sediment deposition limited to localised drainage systems. Large-scale drainage systems, such as that feeding the Pennine Basin in Britain [53], and the smaller-scale systems supplying the Shannon Basin in Ireland [54,55] evolved subsequently in the Pennsylvanian.

A marine transgression during the Tournaisian (358.9–346.7 Ma), e.g., [56–58] coincided broadly with a phase of (N–S) crustal extension that led to basin development in Ireland and Britain [53,59]. Initial rifting during the Tournaisian and early Viséan (346.7–330.9 Ma), was followed by slow subsidence and a phase of tectonic quiescence, facilitating the development of a series of shallow carbonate platforms and intervening intracratonic basins [53,60,61], including the Northwest Carboniferous Basin, which spans most of northwest Ireland (Figure 1a). The Northwest Carboniferous Basin lies unconformably on Neoproterozoic (Dalradian Supergroup) metasedimentary basement and was infilled by basal clastics which quickly developed into a predominantly carbonate-dominant succession [52,62,63] in an overall transgressive sequence.

A regional lowstand event during the mid-Viséan [64], is interpreted as the driver of the deposition of the Mullaghmore Sandstone Formation (MSFm) in the Northwest Carboniferous Basin. This distinct phase of clastic input is represented by thick channelised sandstone beds with highly erosive bases [49,65–68]. The Mullaghmore Sandstone Formation is widely occurring and outcrops at various locations in northwest Ireland from County Mayo in the west to counties Donegal and Fermanagh in the north and east, respectively [49,64,67–69]. It is estimated to be c. 84 m thick along the coast at Carrowmoran in County Sligo [64].

The MSFm contains miospores belonging to the TS Biozone (*K. triradiatus–K. stephanephorous*) [70,71] and foraminifera, suggesting placement in Mississippian Foraminiferal Zone (MFZ) 11 [49,72]. The overlying carbonate units (represented in County Mayo by the Ballina Limestone Formation; Figure 1b) belong to MFZ12. Taken together, these biostratigraphic data suggest the MSFm is late Arundian in age.

A semi-arid paleoclimatic regime has generally been proposed for the early Carboniferous in Britain and Ireland [73,74]. Falcon-Lang [75] suggested a seasonal tropical climate for much of the Tournaisian and early Viséan (up to, and including, the Arundian), with periods of heavy monsoonal precipitation. These wet and dry seasons do not, however, appear to have occurred in regular annual cycles and were likely on a longer cycle-length than monsoonal climates today (in particular the arid phases), as evidenced by growth rings preserved in fossil wood. Short phases of increased humidity have been proposed intermittently throughout this interval, including in the latest Arundian [73]. Paleoclimatic oscillations and cyclicity becomes more prominent above this level, towards the upper Viséan [74], with fluctuation between semi-arid and humid conditions and an increase in amplitude of glacio-eustacy. The MSFm was thus deposited during a broader phase of marked paleoclimatic transition in the Viséan, associated with the progressive onset of the Late Paleozoic Ice Age [52,76–78].

Abundant plant fossils in the MSFm, including in situ rootlets, suggest a vegetated landscape during the Arundian, predominantly of lycopsids and conifers [75]. Wildfires in the dry arid periods are evidenced by abundant fusain (fossil charcoal) fragments in the MSFm and associated sequences [65,75,79,80]. Nichols and Jones [21] described a fusain-rich (20%) horizon in County Donegal and interpreted it as the result of a regionally extensive wildfire during the early Viséan that is believed to have covered a vast area. Subsequent work by Graham [67], concluded that these fusain rich beds were not laterally traceable and rather deposited in various horizons within the Viséan stratigraphy. While a single catastrophic wildfire event is concluded unlikely, substantial recurring wildfires remained common in the Viséán.

Fusain-rich beds are present in the MSFm at Mullaghmore Head (Sligo) and also in north Mayo at Bunatrahir West, along with the upper parts of the stratigraphically underlying Moyny Limestone Formation at Creevagh Head [75]. This suggests that large wildfires were a common and repetitive feature in the Northwest Carboniferous Basin during the early and middle Viséan, and this also appears to have been the case more widely in Europe and North America [22]. Atmospheric oxygen levels were substantially higher during the Carboniferous (perhaps as high as 32%) [81–83], which likely made these wildfires more violent and destructive than observed today.

The section of MSFm at Bunatrahir West (County Mayo) (Figure 1b,c) was studied in detail by Graham [49,64,67] and Falcon-Lang [75,80], and contains mixed marine, fluvial and terrestrial components. It is predominantly clastic in character and is considered the most terrestrially influenced of all the MSFm sections in the Northwest Carboniferous Basin. The base of the MSFm is exposed at this location and is notably highly erosive, cutting c. 4 m into the underlying carbonate sequence and suggestive of a minimum 8 m sea-level drop [64,67]. The sequence at Bunatrahir West contains thick, coarse-grained feldspathic channel sandstones that are erosive and often highly dewatered. Graham [67] suggested that the basal channel widths were decimetric in scale. The channel sandstones are often capped with marine carbonates, indicating channel abandonment in an overall estuarine environment. Large inclined heterolithic strata, representative of migrating, laterally accreting, large (60–90 m) point bars, such as those of meandering rivers on tidal flats, are commonly found in the sequence. These field data suggest paleochannels of 150–200 m width. The cause of this increase in river width is not obvious but may be due to system evolution and a relatively large sea level drop.

Hummocky cross-stratification is common in the marine section within interbedded siltstones and sandstone beds and suggests storm influence. Marine fossils (brachiopods, gastropods, corals) and trace fossils are also present [67]. Paleosols are also intermittently present, with plant fossils (including rootlets) common. Regional relative fluctuations in sea-level indicated by transgressive and regressive surfaces are quite local in character and thus can be attributed to lateral facies change in the coastal environment [67].

Field observations from cross-stratification and mineralogical composition of the MSFm at Bunatrahir West suggest a source to the NW, comprising mixed igneous (likely felsic) and metamorphic rocks (likely the Dalradian Supergroup, widely exposed today across the NW British Isles) [67]. Anders et al. [48] applied multi-proxy provenance analysis at various locations of the MSFm across northwest Ireland, using Pb-in-K-feldspar, zircon and apatite U-Pb geochronology, and trace elements in apatite. Three broad detrital populations were discerned, all deriving from the northwest (Figure 2). The oldest population is Archean to Paleoproterozoic in age and is likely sourced from the Lewisian of the Outer Hebrides–Stanton Banks and/or Nagssugtoqidian belt in Greenland. A Paleoproterozoic to Mesoproterozoic (1.8–0.9 Ga) population is the most dominant in all outcrop locations and is interpreted as sourced from offshore highs such as the Rockall Bank, Porcupine Bank, Rhinns Complex and also the Annagh Gneiss Complex, onshore Ireland. The youngest Proterozoic population derives from Caledonian-associated granites from northwest Ireland and a large amount of recycled Dalradian Supergroup detritus.

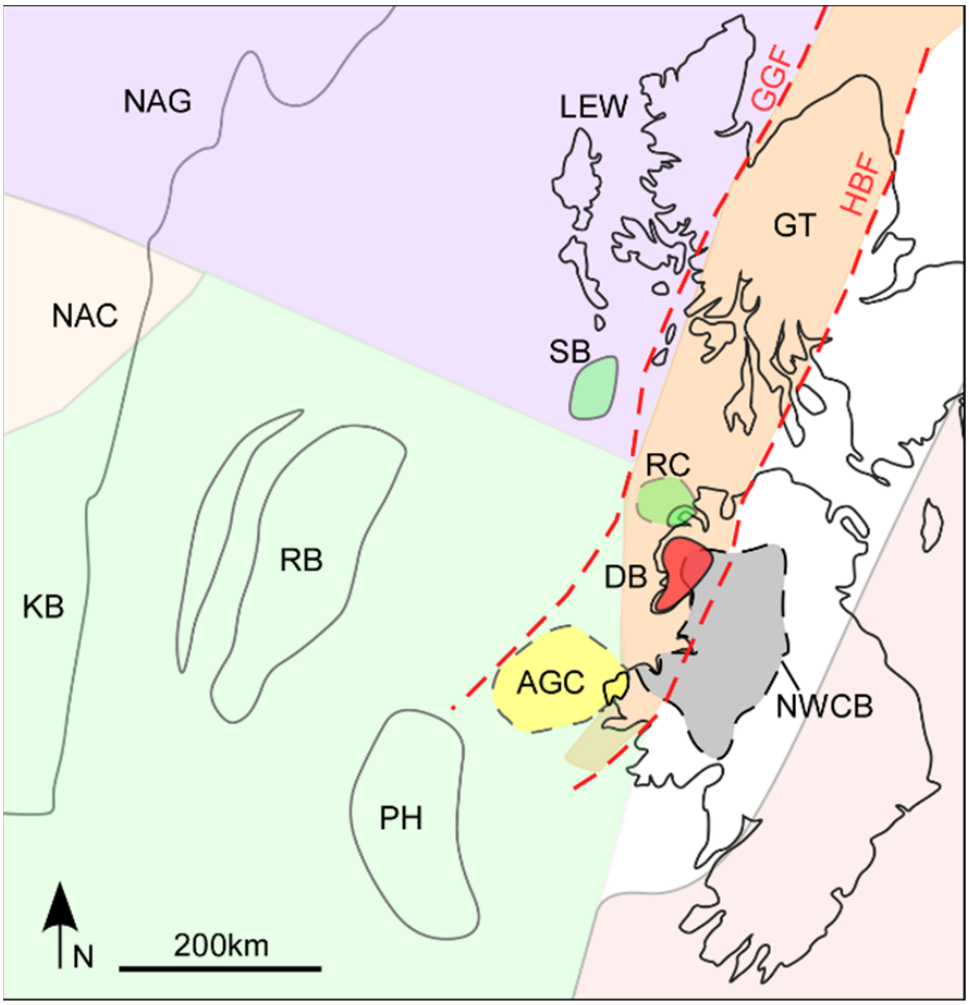

Figure 2. Potential northern source terranes after Anders et al. [48]. NAG: Nagssugtoqidian; NAC: North Atlantic Craton; KB: Ketilidian Belt; LEW: Lewisian; SB: Stanton Banks; RC: Rhinns Complex; RB: Rockall Bank; PH: Porcupine High; ACG: Annagh Gneiss Complex; DB: Donegal Batholith; GT: Grampian Terrane; GGF: Great Glen Fault; HBF: Highland Boundary Fault; NWCB: Northwest Carboniferous Basin.

2. Materials and Methods

2.1. Sedimentology and Petrography

The Viséan-aged Mullaghmore Sandstone Formation (MSFm) onshore in the Northwest Carboniferous Basin offers excellent outcrop exposure and accessibility and is used to investigate temporal variation in provenance signatures within the sequence. Discrete channel sandstone facies packages (units) repeat throughout the sequence, reducing the bias that facies variation can introduce. Spatial variation bias was reduced by targeting a single continuous sequence of the MSFm, exposed just west of Ballycastle in County Mayo at Bunatrahir West (54°18′31.6″ N, −9°23′35.6″ W; see Figure 1c). This approach thus aims to isolate and reveal the temporal variations in sediment delivery within this ancient fluvial system.

The sequence was logged at cm-scale resolution (Figure 3), and a total of five channel sandstone packages were identified (termed units 1–5 in ascending stratigraphic order; Figures 3 and 4a). A sample was taken from near the base of each of these units (sample 1 was taken from the base of unit 1, sample 2 from unit 2, etc.) for consistency and subsequent analysis. Provenance data from sample 1, from the basal channel sandstone, was previously reported [48] and is used again here.

Standard thin sections were prepared for petrographic analysis. Point-counting was completed using a binocular microscope and the PetrogLite software.

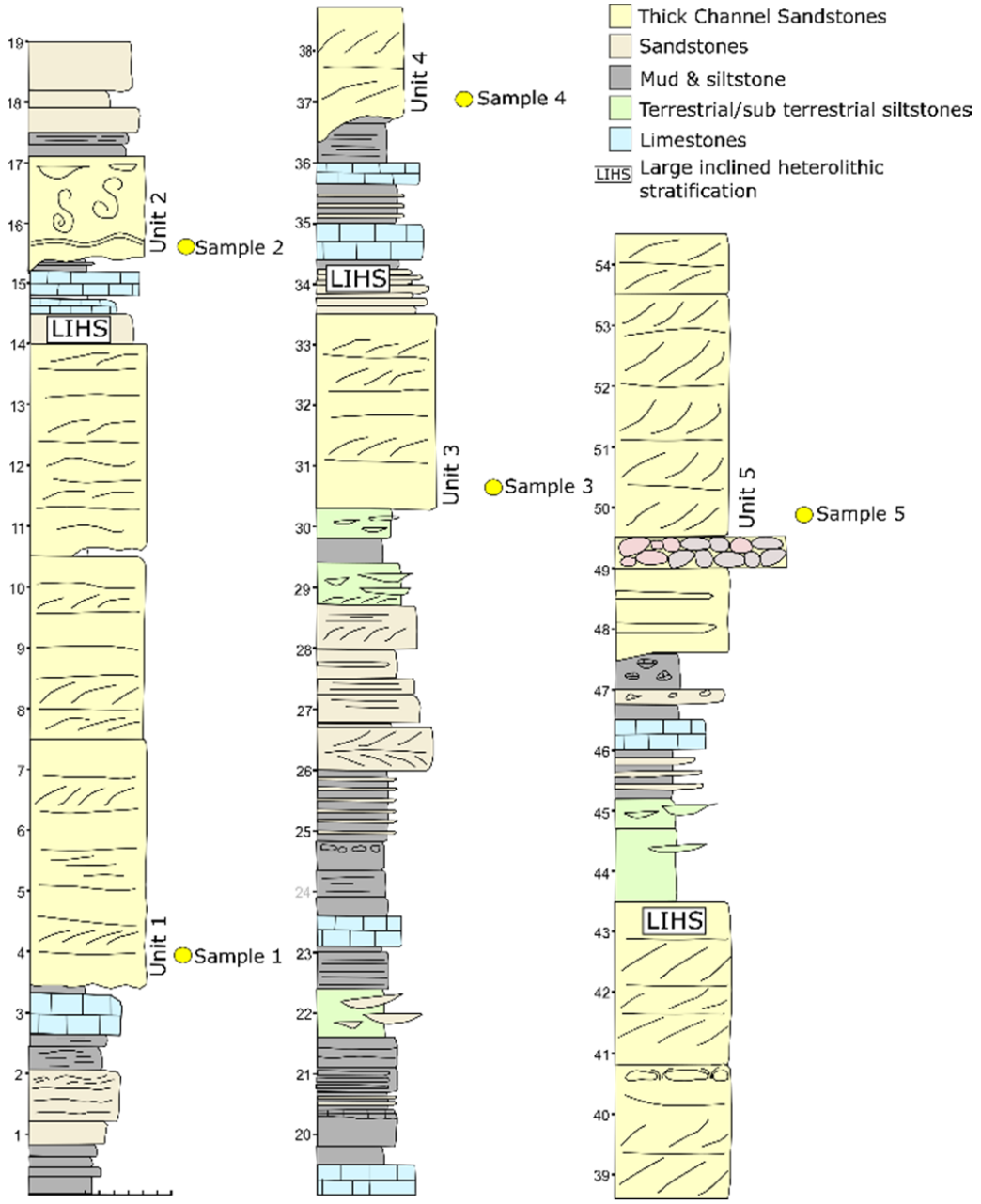

Figure 3. Log of the Mullaghmore Sandstone Formation west of Ballycastle in North Mayo. Sample locations are indicated—these are located in the base of five prominent channel sandstones.

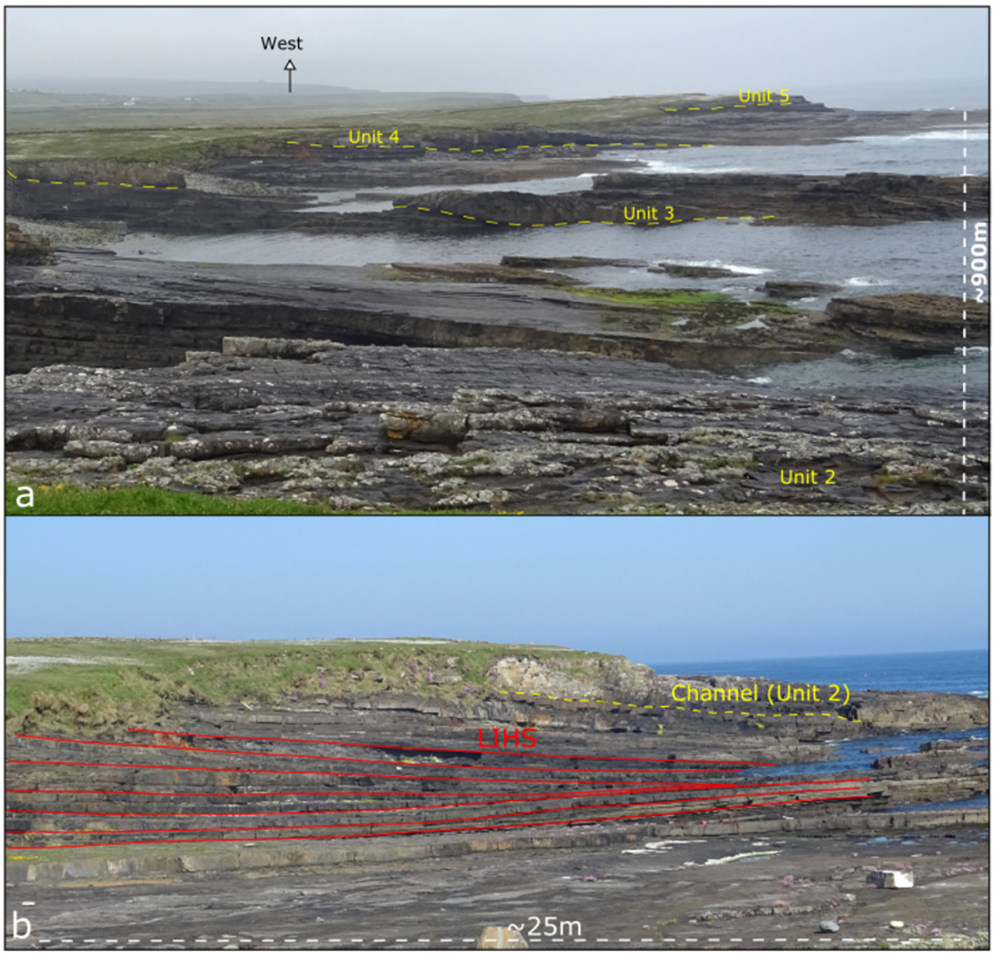

Figure 4. Facies architecture in the Mullaghmore Sandstone Formation at Ballycastle. (**a**) Field photograph taken standing on unit 2, looking broadly showing the position of several channel sandstone units; the bases of these units are indicated with dashed yellow lines. (**b**) Large inclined heterolithic surface (LIHS) below channel sandstone unit 2 (compare with +13 m to +16 m interval on log in Figure 3).

2.2. Pb-in-K-Feldspar Analysis

For Pb-in-K-feldspar analysis, 300 µm thin sections were used. K-feldspars were first identified and mapped using a Hitachi TM3030 tabletop scanning electron microscope (SEM) using BSE (back scatter electron) and EDS (Energy Dispersive X-ray Spectroscopy) functions. In situ analysis of selected grains was carried out using a ThermoScientific Neptune MC-ICPMS with an all-Faraday cup detector configuration, coupled to a Teledyne Cetac Analyte G2 193 nm laser system, at the National Centre for Isotope Geochemistry at University College Dublin. The laser was operated with a fluence of 4 mJ cm^{-2} and a 20 Hz repetition rate. Spot size for unknowns ranged from 30 to 100 µm, depending on grainsize. Analytical approach followed the procedure of Tyrrell et al. [84] measuring ^{204}Pb, ^{206}Pb, ^{207}Pb and ^{208}Pb isotopes alongside ^{202}Hg, which is necessary to correct for isobaric interference of ^{204}Hg on ^{204}Pb. A sample-standard bracketing approach was employed, with the primary standard (NIST612 synthetic soda-lime glass) analysed after every third unknown. Shap K-feldspar was used as the secondary reference material [85], treated as an unknown, and analysed after every 12 unknowns to assess data quality. Mass bias fractionation corrections were carried out by measuring $^{203}Tl/^{205}Tl$ ratios (reported value = 0.418922) in each of the primary standard analyses used for bracketing. Between each bracketing, a linear step-like fractionation between each NIST612 is assumed. A

fractionation correction value was calculated and applied for each of the 3 unknowns between primary standards.

Data reduction was completed with an in-house Excel spreadsheet, and $^{207}Pb/^{204}Pb$ and $^{206}Pb/^{204}Pb$ isotopic ratios are graphically reported. Full isotope ratio data of unknowns and standards are available in the Supplementary Materials. Single data plots for Pb-in-K-feldspar samples are shown in Supplementary Materials Figure S1.

2.3. Apatite and Zircon Analysis

Sample preparation consisted firstly of whole rock crushing, using a jaw crusher at NUI Galway. Samples were subsequently sieved into 64–125 µm size fractions. Standard heavy mineral separation procedure using lithium polytungstate (with a density of 2.85 g/cm^3) was applied, followed by magnetic separation. Apatite and zircon grains were hand-picked from the non-magnetic separate under a binocular stereomicroscope. Grains were mounted in epoxy resin, ground to expose the grain interiors, and polished. Catholuminescence (CL) imaging was performed on zircon grains at iCRAG labs in Trinity College Dublin using a Tescan Tiger, which aided in targeting grain cores during analysis.

Zircon and apatite data were acquired at the iCRAG Labs at Trinity College Dublin using an Agilent 7900 Q-ICPMS coupled to a Photon Machines Analyse Excite 193 nm ArF Excimer laser with a Helix 2 volume ablation cell. The laser was operated at 2.31 J/cm^2 with a repetition rate of 11 Hz. Spot sizes were 60 µm for apatite and 24 µm for zircon. The primary reference material used for apatite was Madagascar apatite [86], while secondary reference materials were McClure Mountain and Durango apatite [87,88]. For zircon analysis, the primary reference material 91,500 zircon [89] was used, and WRS-1348 and Plešovice zircon [90,91] acted as secondary reference materials. These reference materials were analysed in blocks after every 30 unknowns. Isotopes measured for apatite and zircon geochronology were $^{207}Pb/^{206}Pb$, $^{206}Pb/^{238}U$ and $^{207}Pb/^{235}U$.

Data reduction for both apatite and zircon U-Pb geochronology was completed using the Iolite plugin for the Igor Pro software [92]. For apatite data, the VizualAge UcomPbine Data Reduction Scheme (DRS) [93] was used, which corrects for variable common Pb in the primary reference material. For zircon data, the VizualAge DRS [94] was applied. A downhole fractionation correction was calculated from the primary standard, which was then applied to all unknowns.

Zircon data were filtered for discordancy using a probability of concordance threshold of >0.001, determined by the Concordia Age formula of Isoplot v4.15 [95]. Apatite grains, however, are virtually always inherently discordant due to the typical presence of significant common Pb, which readily substitutes for Ca in the apatite crystal lattice. An iterative ^{207}Pb-based correction following Chew et al. [96] was thus applied. This approach uses an initial estimate for the $^{207}Pb_c/^{206}Pb_c$ ratio of each grain to calculate an initial age; the process is then iteratively applied using the terrestrial lead evolution model of Stacey and Kramers [97] to obtain a final age. An age uncertainty filter is then applied to all grains following the approach of Mark et al. [98], accepting only those as follows: >2 Ga, $\leq$10% uncertainty; 2–1 Ga, $\leq$15% uncertainty; 1–0.5 Ga, $\leq$20% uncertainty; and <0.5 Ga, $\leq$25% uncertainty. U-Pb data are reported graphically using KDEs plotted using the open-source statistical program R [99].

Apatite trace element data were acquired simultaneously with the U-Pb isotope data and followed the same procedure. Trace element masses measured were: ^{55}Mn, ^{88}Sr, ^{89}Y, ^{90}Zr, ^{139}La, ^{140}Ce, ^{141}Pr, ^{146}Nd, ^{147}Sm, ^{153}Eu, ^{157}Gd, ^{159}Tb, ^{163}Dy, ^{165}Ho, ^{166}Er, ^{169}Tm, ^{172}Yb, ^{175}Lu, ^{232}Th and ^{238}U. NIST612 was the primary reference material employed during trace element data reduction, and an aliquot of Durango apatite was the secondary reference material [100]. Apatite trace elements were reduced using the Iolite Trace Element DRS, employing the internal elemental standardisation approach of Woodhead et al. [101] using ^{43}Ca, set to the stoichiometric content of apatite (40 wt%). Trace element data are fully reported in the Supplementary Materials.

Trace element data were assessed using the approach described by O'Sullivan et al. [102], which uses a reference dataset of c. 360 bedrock samples to feed a machine learning classifier algorithm (support vector machine), which in turn provides an estimate of likely source lithology of the detrital apatite from the input trace element data. Source lithologies are classified as:

- HM (High-grade metamorphic);
- LM (Low-grade metamorphic);
- I + M (I-type granitoids and mafic igneous);
- UM (Ultramafic igneous);
- S (S-type granitoids);
- ALK (alkali rich igneous).

Detrital apatite compositions versus the composition of apatite of known provenance are matched in Sr/Y vs ΣLREE (sum of La, Ce, Pr and Nd) space [103]. For ease of visualisation and comparison between samples, the proposed source lithologies of detrital grains are reported graphically on pie charts.

Apatite and zircon are both valuable U-Pb geochronometers and almost ubiquitous in clastic sedimentary rocks; however, their true power as detrital proxies lies in the combined application of U-Pb geochronology and trace elements. Zircon is one of the most robust minerals in clastic systems and can survive several sedimentary cycles [104–108]. In contrast, apatite is more labile [104,108,109]. The U-Pb system in zircon has a closure temperature of >900 °C [110,111], whilst the apatite U-Pb closure temperature lies between 400 °C and 550 °C [112–114] for typical grain sizes and cooling rates. This has profound effects on interpreting data, as the original U-Pb crystallisation age of apatite is easily reset by reheating or recrystallisation during subsequent metamorphic events [112,115,116]. When geochronology is coupled with apatite trace element analysis (re)crystallised (i.e., metamorphic) grains can typically be differentiated from primary apatite [102,103]. This allows for provenance information to be garnered from zircon-poor terranes, such as mafic and ultramafic sources, as well as relatively low-grade metamorphic terranes that commonly occur within orogenic belts, significantly enhancing provenance data and subsequent interpretations.

3. Results

3.1. Field Sedimentology

The section at Bunatrahir West exposes c. 52 m (stratigraphic thickness) of the Mullaghmore Sandstone Formation (MSFm), with a conspicuous erosive, 10 m thick multi-storey channel sandstone unit marking the base of the formation (Figure 3). The MSFm sequence at this location is dominated by these particular facies; as noted previously, five of these erosive-based channel sandstone units were identified (termed units 1–5 in ascending stratigraphic order). These units are defined as medium-grained cross-stratified, feldspathic and micaceous multi-storey channel sandstones (Figure 5a). Dewatering structures and plant material are common, especially near the base of channels, often revealing iron precipitation and a rusty red appearance associated with pyrite oxidation within plant material as well as fusain (Figure 5b,c).

A clast-supported polymict conglomerate bed is present just below the last channel sandstone (unit 5) in the Bunatrahir West section. It has a mildly erosive base, and clasts range from pebble- to cobble-size, with clast imbrication suggesting flow from northwest to southeast. The clasts themselves are predominantly composed of rip up clasts of intraformational mudstone, micrite, limestone and sandstone. Large inclined heterolithic strata are evident throughout the sequence (Figure 4b). These are large-scale cross-stratified barform structures, representative of a meandering channel within tidal flats. The preserved 3-dimensional channel orientation, cross-stratification and clast imbrication all suggest an original flow direction from the northwest.

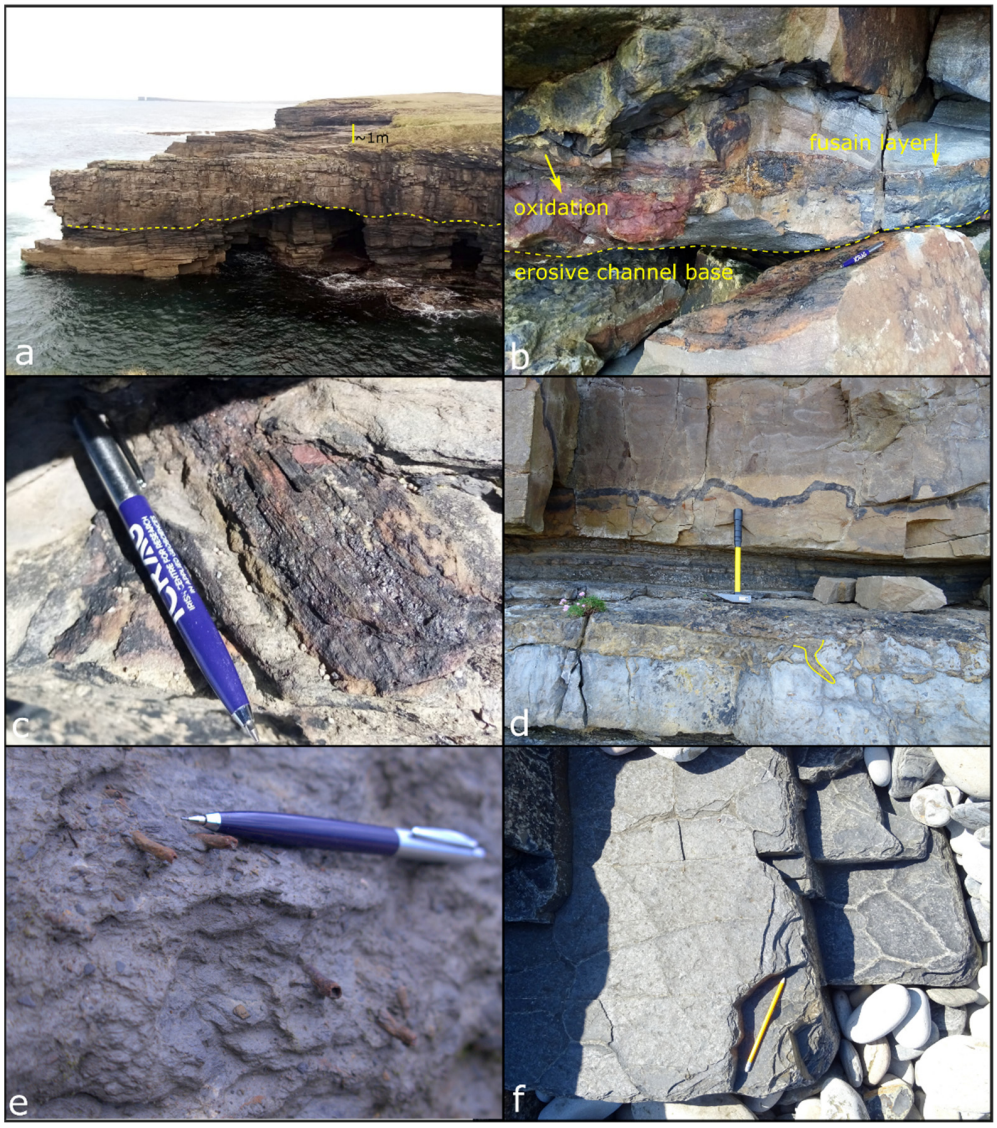

Figure 5. Sedimentological features and plant fossil material in the Mullaghmore Sandstone Formation at Ballycastle. (**a**) Typical large-scale channel sandstone with irregular and erosive base. (**b**) Base of erosive channel containing fusain layer at base. Oxidation likely due to pyrite within plant material. (**c**) Fusain preserved in sandstone unit. (**d**) Coal seam in sandstone bed. Bioturbation and large-scale burrows present in underlying micritic carbonate bed (highlighted in yellow) (**e**) In situ plant rootlets preserved in paleosol horizon. (**f**) Mudcracks.

Plant material is extremely common throughout this sequence and includes examples of the arborescent lycopsid *Lepidodendron*. A coal seam (Figure 5d) is present in unit 2 directly above a thick (1.2 m) paleosol horizon containing in situ plant rootlets (Figure 5e). The fluvial channels often erode into beds with abundant plant debris. Mudcracks are also evident (Figure 5f), further indicating intervals of sub-aerial exposure.

3.2. Petrography

All sandstone samples from the Mullaghmore Sandstone Formation (MSFm) at Bunatrahir West are moderately sorted and coarse-grained, with generally angular grains (Figure 6). Feldspar and quartz are the most abundant detrital minerals (with 38–58% modal abundance), and all samples/units are classified after Pettijohn et al. [117] as arkosic arenites. Sample 1 is the most quartz-poor and feldspar-rich unit: 58% of grains are

feldspars, and these comprise orthoclase (59%), microcline (19%), plagioclase (13%) and perthite (9%).

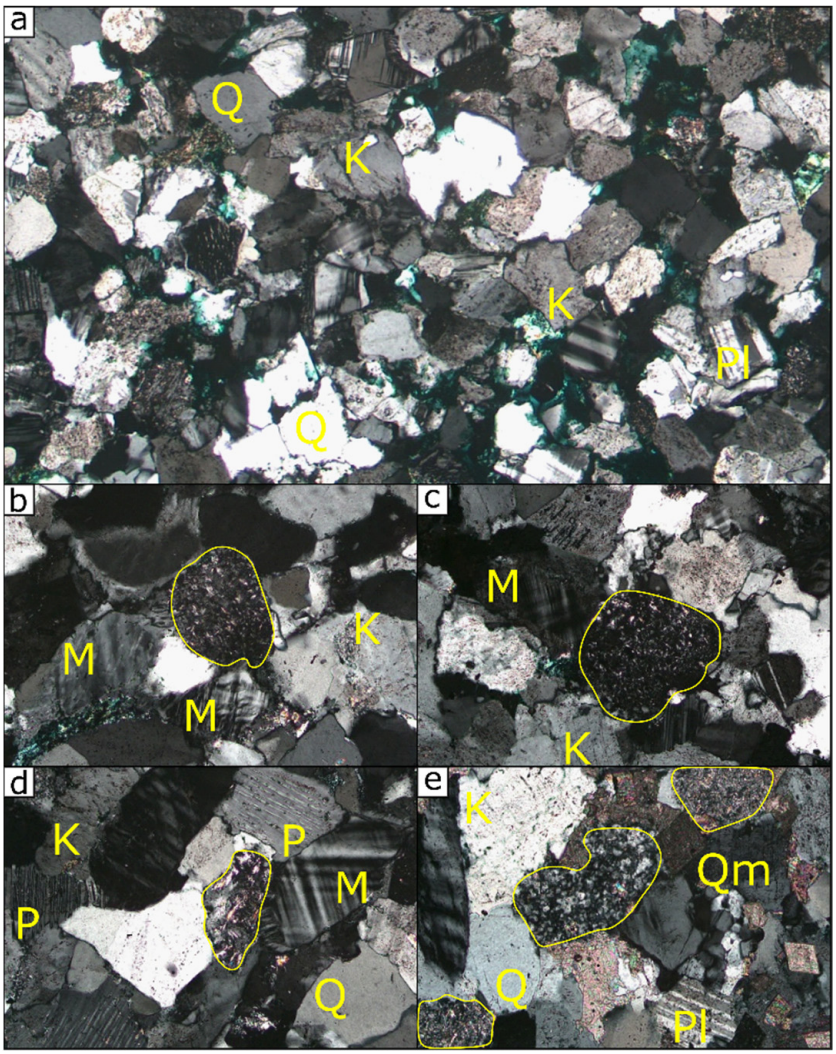

Figure 6. (**a**) Typical K-feldspar rich nature of the Bunatrahir West sequence, where Q: quartz; K: K-feldspar; Pl: plagioclase; M: microcline; P: perthite; Qm: microcrystalline quartz. Field of view c. 2 mm; (**b**–**e**). Detrital igneous grains of varying appearance. Field of view c. 0.4 mm.

Orthoclase is the most common feldspar in all MSFm samples, followed by microcline. Plagioclase and perthite are also typically present in equal amounts, except in sample 1 (noted above) and sample 3, where plagioclase is slightly more abundant than perthite. Accessory muscovite and biotite (<1%) are present in all samples, and detrital rock fragments of felsic igneous composition are also common (Figure 6). A minor amount of calcite cement is present only in sample 2 (7%).

3.3. Pb-in-K-Feldspar Analysis

Three main grain populations (and two sub-populations) are identified in the Mullaghmore Sandstone Formation (MSFm) sequence (Figure 7), similar to Anders et al. [48], which are associated with source domains as follows:

- *Fpop1a* corresponds to the Nagssugtoqidian;
- *Fpop1b* corresponds to the Lewisian, such as the Stanton Banks;
- *Fpop2a* corresponds to offshore highs in the northeast Atlantic, such as the Rockall Bank, Porcupine Bank and the Rhinns Complex;

- *Fpop2b* corresponds to the Annagh Gneiss Complex;
- *Fpop3* corresponds to Caledonian granitic suites such as the Donegal Batholith.

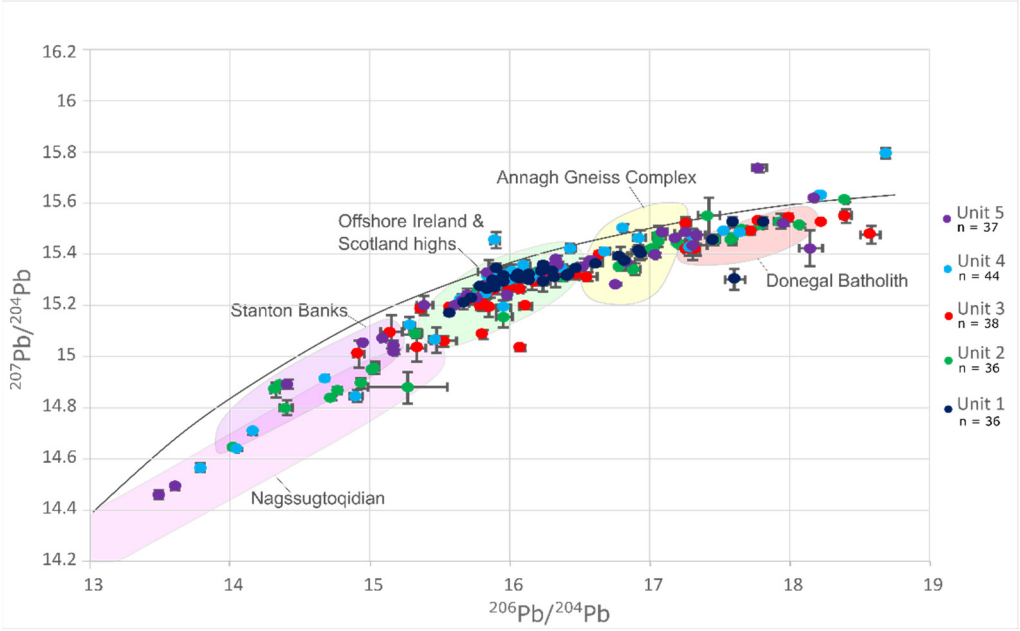

Figure 7. $^{206}Pb/^{204}Pb$ versus $^{207}Pb/^{204}Pb$ Pb-in-K-feldspar isotopic ratios for K-feldspars from the five channel sandstones in the Mullaghmore Sandstone Formation at Ballycastle (see channel key on right of plot). Pb evolution curve after Stacey and Kramers [97] indicated. Plotted error bars are 2δ.

All samples vary in relative abundance of detritus from each domain. Most notably, the Nagssugtoqidian domain is sourced in samples 2, 4 and 5. *Fpop2a* is most prevalent in all samples, with the exception of sample 2 where there are significantly less *Fpop2a* grains than in all other samples. The amount of *Fpop1b*, *Fpop2b* and *Fpop3* grains fluctuates with all samples (Figure 7).

3.4. Zircon U-Pb Geochronology

Three main grain populations are discerned (Figure 8), with results again similar to Anders et al. [48]:

- *Zpop1* comprises Archean-aged grains;
- *Zpop2* comprises grains of Paleoproterozoic to Mesoproterozoic age;
- *Zpop3* comprises grains of Paleozoic age.

Zpop1 is present in negligible amounts in sample 1 yet present in all stratigraphically higher samples. The average ages of these grains become increasingly older with each successive (progressively younger) sample; the Archean population in sample 2 peaks at 2.65 Ga and sample 5 yields the oldest zircon ages, peaking at 2.8 Ga.

Zpop2 is by far the most abundant zircon age component in all samples. Various major age peaks are present at 1.8 Ga, 1.75 Ga, 1.65 Ga, 1.5 Ga, 1.45 Ga, and 1.1 Ga. These vary in dominance with each sample. The 1.8 Ga peak is only present in samples 3 and 4. The 1.75 Ga peak is dominant in samples 1, 3, 4 and 5. The 1.65 Ga component is most conspicuous in sample 2. Sample 3 has a 1.5 Ga component, whereas sample 5 has a 1.45 Ga component. The 1.3 to 0.9 Ga aged grains are present in all samples, peaking ~1.1 Ga and are most abundant in samples 3 and 5.

Zpop3 is present in variable amounts in all samples. This population is almost absent in sample 1 but is very prevalent in sample 3. *Zpop3* is a minor yet significant component in samples 3, 4 and 5.

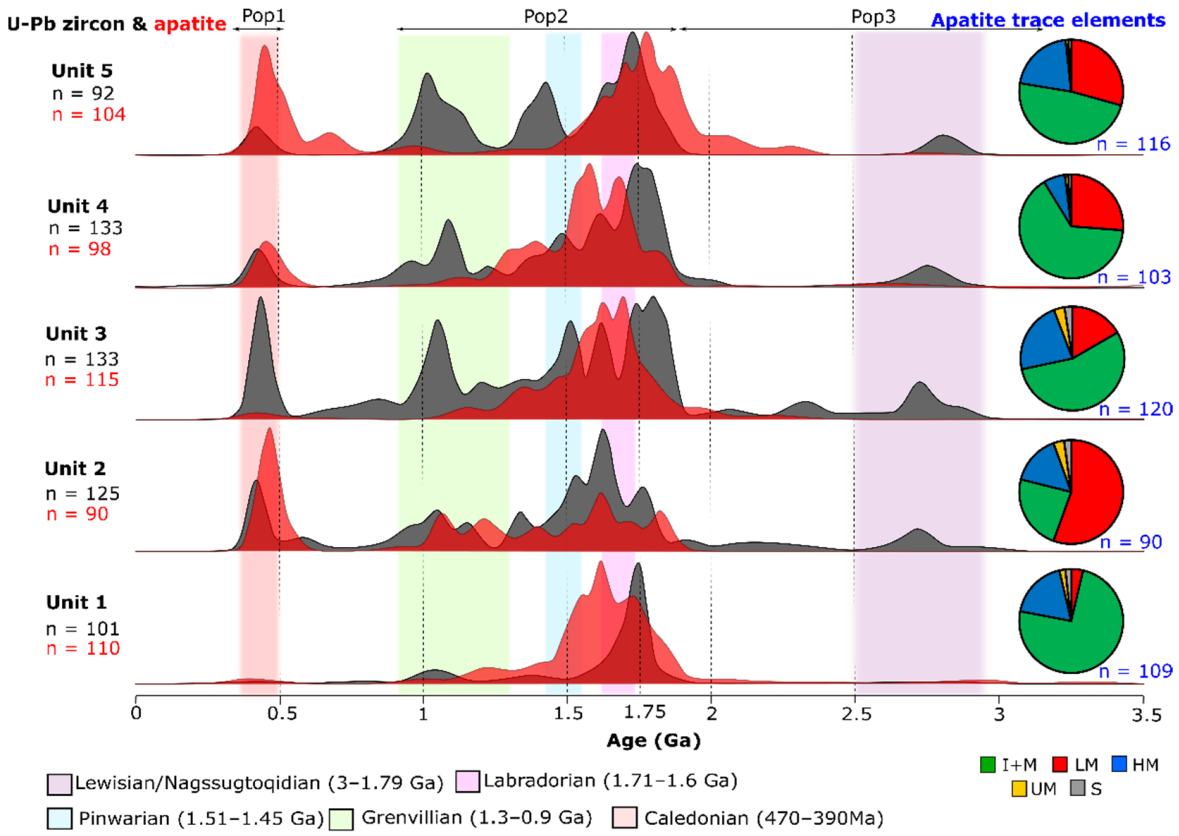

Figure 8. Zircon and apatite U-Pb geochronology results from all channel units in the Mullaghmore Sandstone Formation on Kernel Density Estimates. Bin size is 30 Myr. Major orogenic events are highlighted in the vertical pastel colour bands. Trace elements in apatite visualised on pie charts on far right with key below where I + M: Igneous and mafic; LM: low-grade metamorphic; HM: high-grade metamorphic; UM: ultramafic; S: S-type granitoid.

3.5. Apatite U-Pb Geochronology

Two main populations are present in apatite U-Pb data (Figure 8), similar to previous findings by Anders et al. [48]:

- *Apop1* Archean detritus is present in negligible amounts;
- *Apop2* comprises Paleoproterozoic to Mesoproterozoic grains;
- *Apop3* comprises Paleozoic grains.

Apop2 is the most abundant component in all samples from the Mullaghmore Sandstone Formation (MSFm) at Bunatrahir West. Major age peaks at 1.8 Ga, 1.75 Ga, 1.6 Ga, and 1.55 Ga are present that vary in dominance in each sample. Sample 5 contains the most Paleoproterozoic grains, ranging from 2.4 to 1.6 Ga in contrast to all other samples, which contain a minor 1.9 Ga component, and dominant 1.75 Ga and younger components.

Apop3 is almost absent in samples 1 and 3, while very prevalent in samples 2 and 5. A significant amount of *Apop3* is present in sample 2.

3.6. Trace Elements in Apatite

Apatite trace element data from the Mullaghmore Sandstone Formation (MSFm) at Bunatrahir West reveal five types of source lithology: LM = Low-medium grade metamorphic; HM = High-grade metamorphic; I + M = I-type and mafic igneous; UM = Ultramafic; S = S-type granitoids (Figure 8).

I + M sources are most common in all samples, followed by LM and HM sources, bar sample 2 where LM sources are most common. UM sources are almost absent in all samples and S-type sources are very minor. Sample 1 comprises mainly I + M type grains and has

a low amount of metamorphic apatite (~22%). Sample 2 contains the highest amount of metamorphic apatite (~75%). Metamorphic apatite varies from ~35 to 50% in all other samples. The correlation of source lithology with apatite U-Pb age is undertaken in the discussion below.

4. Discussion

4.1. Provenance of the Mullaghmore Sandstone Formation

All provenance proxies and sedimentological observations indicate sediment sourcing from the northwest, similar to the study of Anders et al. [48] from other locations of the Mullaghmore Sandstone Formation (MSFm) in the Northwest Carboniferous Basin (counties Sligo and Donegal, which lie to the east and northeast, respectively). While the volume of detritus from various source terranes varies, the sourcelands for sediment appear to remain broadly similar.

The U-Pb zircon spectra suggest Archean sources (~2.75 Ga), most likely ultimately derived from remnant cratons in Greenland and Scotland (North Atlantic Craton and Lewisian Complex, respectively), or from the Rockall Bank [118]. These U-Pb ages are not a significant population in the apatite data, likely due to original U-Pb ages overprinted by subsequent orogenic events or the dissolution of these grains as a result of weathering, transport and lag time in the sedimentary system during the Carboniferous. K-feldspar data confirm only minor amounts of detrital grains derived from the Nagssugtoqidian and Lewisian domains, which would be the source of the zircon and rare apatite grains with Archean ages.

The most abundant detrital peaks in both the U-Pb zircon and apatite spectra are Paleoproterozoic (1.8–1.75 Ga and 1.65 Ga) to Mesoproterozoic (1.5 Ga and 1.1 Ga) ages. Likely Paleoproterozoic sources are the 1.9–1.8 Ga Nagssugtoqidian [119–122]; 1.8 Ga Stanton Banks [123]; 1.75 Ga Rockall Bank [118]; 1.75 Ga Annagh Gneiss Complex [124]; and the 1.9–1.7 Ga Rhinns Complex [125]. Paleoproterozoic to Mesoproterozoic sources could include the 1.8–1.3 Ga Porcupine Bank [126], which yields Grenville ages; however, it is only a minor peak in the U-Pb apatite dataset. These prominent age peaks directly compare to Pb-in-K-feldspar data, where populations corresponding to offshore highs such as the Rockall Bank, Rhinns Complex and Porcupine Bank are most abundant. These source terranes were likely located in the same broad region during their formation in the Proterozoic, hence their relative proximity today, similar U-Pb crystallisation ages and their indistinguishable K-feldspar Pb isotopic chemical fingerprints. The Annagh Gneiss Complex exhibits slightly more radiogenic Pb ratios, and as a result this source can be differentiated in the Pb-in-K-feldspar dataset.

The third and youngest population in all proxies yields Paleozoic apatite and zircon U-Pb ages of 500 to 400 Ma, representative of the Caledonian Orogenic Cycle, e.g., [127]. Pb-in-K-feldspar data again complement this by revealing the most radiogenic grains plotting in the Donegal Batholith domain, which have Silurian to Devonian U-Pb zircon ages of 430–400 Ma [128]. U-Pb geochronology and trace elements in apatite also suggest some detritus is sourced from the Dalradian Supergroup, which yields Caledonian (overprinting) ages and metamorphic trace element characteristics similar to previous findings by Anders et al. [48].

Apatite trace element data use a machine-learning algorithm (support vector machine) that assesses the trace element chemistry of each apatite versus a reference bedrock dataset [102]. The algorithm classifies each detrital grain into its most likely source lithology grouping according to a classification scheme devised by the algorithm from the reference dataset. The most common source lithologies are I-type granitoids and mafic igneous source rocks, the majority of these yielding Paleoproterozoic to Mesoproterozoic U-Pb ages (Figure 9), which we can safely attribute to the Laurentian continent. High-grade metamorphic apatite is most commonly sourced from the Paleoproterozoic to Mesoproterozoic. These Paleoproterozoic to Mesoproterozoic metamorphic apatites are likely sourced from orogenic belts such as the 1.92–1.8 Ga Trans Hudson [129], 1.8 Ga Ketilidian belt [130], and

the 1.71–1.62 Ga Labradorean [118], 1.51–1.45 Ga Pinwarian [131] and 1.3–1 Ga Grenville belts [132]. LM apatite is most common in the Paleozoic and formed during the Caledonian (475–390 Ma) orogeny. S-type granitoids and ultramafic sources are negligible.

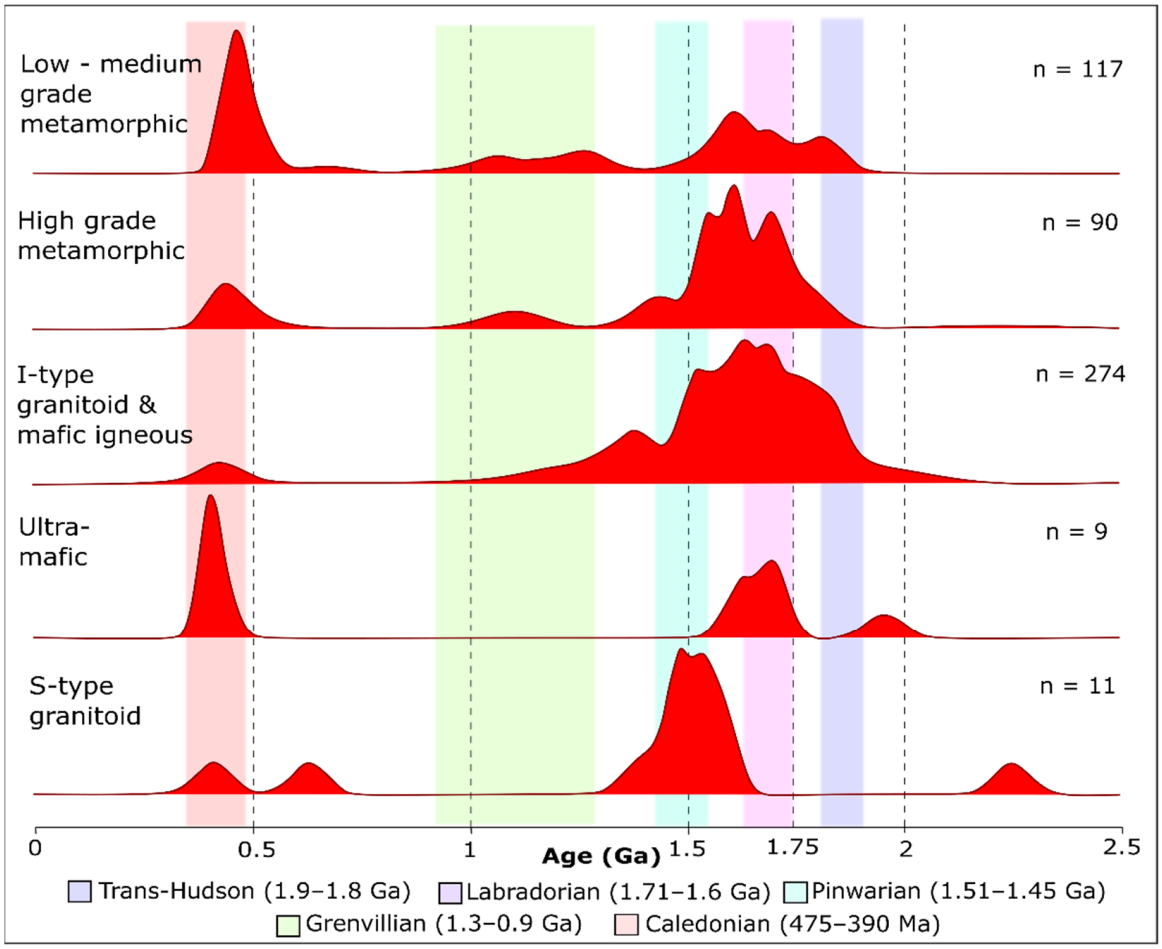

Figure 9. Kernel density estimates of basement terrane lithology from trace elements in apatite plotted against age. All samples from the five channel sandstone units in the Mullaghmore Sandstone Formation at Ballycastle are plotted together. Major orogenic events highlighted in vertical colour bands. Bin size is 30 Ma.

When comparing U-Pb geochronology data, clear variations are evident; the apatite U-Pb shows somewhat more variation in provenance signal than zircon U-Pb data. Certain inherent factors can cause this trend. Zircon crystallisation is relatively rapid and spans a short period as high crystallisation temperatures are rarely maintained over long periods. Widespread overprinting of the U-Pb system in zircon cores by (granulite-facies grade) metamorphism is also relatively rare [133], with even high-grade metamorphism most often recorded as zircon rim overgrowths [134,135]. Apatite generally records cooling following prolonged orogenic events that can span millions of years, such as parts of the Grenville Orogeny that stayed above the apatite closure temperature of 450–500 °C for 110 Ma [136]. In comparison, the duration of the Grampian Orogen in Ireland was relatively short where 8 Myr of prograde metamorphism is suggested, with metamorphic rocks almost immediately becoming exposed [137]. Overprinting, variable PT conditions and prolonged cooling add to the complexity of using apatite as a provenance tool, but once understood thoroughly it can yield important and highly diagnostic information for provenance interpretations, potentially even distinguishing various parts of orogenic belts e.g., [48].

Paleoproterozoic to Mesoproterozoic U-Pb apatite data from the MSFm at Bunatrahir West is likely affected by the factors described above. Unit 2 contains the most metamorphic apatite and the least prominent Paleoproterozoic to Mesoproterozoic age peaks. The sources of these grains were likely overprinted and reset with respect to the apatite U-Pb system by Caledonian metamorphism, resulting in a lack of 'original' crystallisation ages and a broad age range as seen in Figure 8. The 465 Ma low-grade metamorphic apatite in the MSFm must be derived from the Grampian terrane, which was affected by the Grampian phase of the Caledonian Orogenic Cycle. A second minor 435 Ma low-grade metamorphic apatite and 425 Ma high-grade metamorphic apatite peak (see Supplementary Materials Figure S2) are also present, which likely represent a similar source, but which experienced Scandian tectonism [48].

4.2. Temporal Fluvial Variation in Provenance Signals

All proxies show a unique signature in the first (and oldest) channelised sandstone (unit 1) in the Mullaghmore Sandstone Formation (MSFm) at Bunatrahir West. Both the U-Pb zircon and Pb-in-K-feldspar data suggest a unimodal source, with zircon ages at 1.75 Ga and subordinately at 1.17 Ga, with feldspar grains plotting in the Annagh Gneiss Complex/offshore highs domain (Figure 7). This source is interpreted as an offshore equivalent of the Annagh Gneiss Complex, due to the K-feldspar Pb isotopic signature spanning the entire Annagh Gneiss Complex and the offshore high domain. U-Pb apatite data also contains this 1.75 Ga age peak (Figure 9) supporting an offshore Annagh Gneiss equivalent source. However, in unit 1, a significant proportion (~50%) of I + M apatite grains yield ages of 1.6–1.5 Ga. By default, this must be a separate source, one not registered in the zircon or feldspar proxies, likely of mafic composition. Long cooling times of (equivalent offshore) Annagh Gneiss apatite (spanning cooling times > 150 Ma) are unlikely to account for these age peaks. HM apatite peaks at 1.6 Ga furthermore suggest a high-grade metamorphic (orogenic) event at 1.6 Ga, which may also be the same source as for the 1.6–1.5 Ga mafic igneous grains. Considering the unimodal source seen in zircon and K-feldspar data, the source is likely local—a proximal mafic 1.6 Ga basement terrane.

The sharp basal boundary of the MSFm at Bunatrahir West, recorded by an erosive base of >4 m and a suggested sea level drop of 8 m [67], is likely due to tectonism and a regional sea-level drop [64]. All provenance data from Unit 1 (a highly erosive 10 m thick channel sandstone facies) support this. The interpreted local unimodal source seen in the Pb-K-feldspar and zircon U-Pb data suggest rejuvenation of the fluvial system due to tectonics (hinterland uplift) and/or a sea-level drop, altering the slope of this fluvial system. Cawood et al. [138] suggested that altering the slope of channels by tectonism causes rejuvenation and incision in the lower reaches of the catchment, altering the headward sediment source to the now-steeper sloped lower catchment. A similar trend is seen in the Millstone Grit of the Pennine Basin where entrenchment of rivers through uplift generates sourcing of the lower reaches of the fluvial system [139]. Alternatively, Unit 1 could simply be a tributary or local fluvial system, although sedimentology would suggest the former is more likely.

Provenance signals change rapidly in subsequent channel sandstone units. A 1.75 Ga zircon age peak remains prominent in all units; however, a 1.8 Ga zircon peak is present in units 3 and 4, and is absent in other units. The 1.6 Ga zircon source is variable in all subsequent units and most prominent in unit 2. In contrast, the apatite 1.6 Ga age peak is least significant in this same unit. A possible explanation for the contrasting zircon and apatite 1.6 Ga age peak in unit 2 could be that the apatite here is of a different, mafic, source. Alternatively, assuming the source is broadly the same basement terrane for both proxies, the lack in Paleoproterozoic to Mesoproterozoic apatite grains in this unit, could be that the dominating Paleozoic apatite (Dalradian Supergroup) population dilutes this signature. Apatite is known to be stable during burial yet susceptible to chemical weathering when exposed in a sedimentary system [140]. Increase in temperature can further increase the

rate of apatite dissolution [141,142]. Zircon, in comparison, is stable under burial as well as during long periods of exposure within a sedimentary system [109].

Grenville-aged zircons increase in abundance from units 1 through to 3 and become a steady contributor of detritus in units 4 and 5. This signal is typical of catchment expansion and channel evolution. Grenville-aged apatite is uncommon throughout, possibly due to low fertility. The fertility of these source terranes in comparison is known to be high for zircon [143]. It is also possible that apatite could have been sourced from Grenville-aged terranes, but the U-Pb signature became overprinted by subsequent Caledonian metamorphism, e.g., Grenville terranes in Svalbard, Barents Sea [144], northwest Ireland where the Annagh Gneiss Complex shows Caledonian overprinting signatures [145] including in apatite U-Pb data [114], and in Scotland where both Grenville and Caledonian metamorphism are evident in some basement terranes [146].

Caledonian-aged zircon detritus varies, with unit 1 containing almost no Caledonian-aged zircons, unit 3 containing a very substantial amount, and units 2, 4 and 5 containing some significant amounts of Caledonian-aged zircons. In the absence of evidence for rapid changes in the hinterland driven by tectonism, the most plausible explanation for this variable trend is channel migration and avulsion. Caledonian-aged apatite is also highly variable in the provenance data, but this trend is due to sourcing from various bedrock terranes. Primary igneous apatite (I + M/UM) is present in minimal amounts in each sample and likely of the same source as Caledonian-aged zircon. Caledonian metamorphic (LM and HM) (re)crystallised apatite is very prevalent in units 2 and 5. Trace elements in apatite indicate the Dalradian Supergroup as a source. This source switched on and off during the growth and development of the fluvial sequence represented by MSFm section at Bunatrahir West. Pb-in-K-feldspar data also show variable amounts of Caledonian-type detritus throughout the sequence; units 2 and 3 contain the highest amounts of these grain types, mirroring the trend seen in zircon U-Pb data. Channel migration, catchment expansion and regional un-roofing are likely causes of the variability in Caledonian-type detritus. It is noteworthy that the entire section of the MSFm in north Mayo contains significantly less Dalradian Supergroup-derived detritus compared to other locations in the same formation father east in the Northwest Carboniferous Basin [48], further suggesting that the sequence at Bunatrahir West (Figure 1b) was a separate drainage system to that of the more eastern sections of the Mullaghmore Sandstone Formation.

Pinpointing the precise causes of the variability in provenance signatures within a relatively short time interval (approximately c. 3 My) in an ancient fluvial system is difficult. The switching on and off of sources is likely caused by channel migration and heavy rainfall during monsoon seasons. The steady increase in Archean and Grenville-aged detritus upsection from unit 2 to 5 is likely caused by catchment expansion and fluvial system development. Other fluctuations (especially the highly inconsistent Paleoproterozoic to Mesoproterozoic sources) could reflect more idiosyncratic events in and around the Northwest Carboniferous Basin, such as mass wasting events flushing sediment from a discrete source terrane. Falcon-Lang [80] reported a 300% increase in feldspar grains in charcoal units and suggested that it marked a change to mechanical weathering. With channels in the MSFm often overlying carbon-rich layers and plant fossils commonly found concentrated in channel bases, it is possible that contemporaneous wildfires influenced channel creation and evolution by the removal of vegetation increasing bank instability, and extreme heat increasing mechanical weathering driving fluvial erosion.

Modern studies of wildfires indicate increased runoff and sediment load in systems affected by wildfire for several years following the event as sediment is no longer stabilised by vegetation [24,26,27]. River morphology is further affected as the catchment area increases, and alluvial fans are both created and rejuvenated, resulting in altered channel gradients (decreasing upstream away from the alluvial fan and increasing downstream) and large amounts of woody plant material delivered to channels [147]. Erosion rates can increase 30-fold [27] to 200-fold [148], dependent on basin morphology and acting processes.

Other authors, e.g., [47,149] have suggested that multiple sampling through the stratigraphy is necessary to gain a thorough understanding of un-roofing history and sediment delivery through time. This study clearly highlights how variable provenance signals can be within consecutive units of channel sandstones facies in an ancient fluvial system.

4.3. Paleoenvironmental and Paleoclimate Considerations for Sediment Provenance

The deposition of the Mullaghmore Sandstone Formation (MSFm) occurred during the Arundian regional substage of the Viséan. During this interval, terrestrial environments were predominantly vegetated by gymnosperms, with arborescent lycopsids and early potential representatives of the conifers present (Figure 10) [75]. The effective co-evolution of land plants and alluvial systems during the Carboniferous is well-established [150] and known to have been dependent on paleoclimate. Falcon-Lang [75] suggested that Tournaisian to early Viséan (including the Arundian) plant communities in Britain may have been representative of a tropical savanna-type biome.

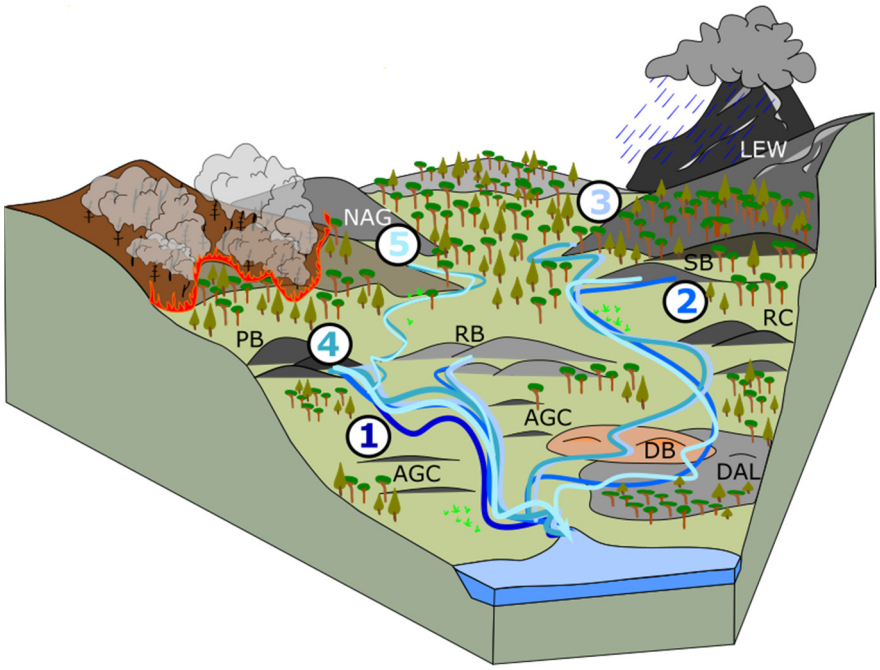

Figure 10. Schematic paleoenvironmental reconstruction of the hinterland sourced by the Mullaghmore Sandstone Formation fluvial system during the Viséan. Various channel-flow regimes are marked 1–5 corresponding to the channelised units sampled. The view is looking northwestward. NAG: Nagssugtoqidian; LEW: Lewisian; SB: Stanton Banks; RC: Rhinns Complex; RB: Rockall Bank; PB: Porcupine Bank; ACG: Annagh Gneiss Complex; DB: Donegal Batholith; DAL: Dalradian.

Plant fossils are commonly preserved in the MSFm at Bunatrahir West (e.g., Figure 5c–e), including several levels with in-situ rootlets. Horizons rich in plant debris are often located below channel sandstone facies (Figure 5b). A little farther east, at Creevagh Head, Falcon-Lang [75] noted abundant fossil wood in the upper part of the Moyny Limestone Formation, which stratigraphically directly underlies the MSFm (Figure 1b). These observations suggest a highly vegetated Viséan landscape immediately prior to and during deposition of the MS.

Large inclined heterolithic strata, suggestive of meandering rivers on shallow slopes, are evident throughout the sequence (Figure 3). Vegetation and resultant riverbank stability plays a vital role in governing river morphology with fluvial systems prior to the Paleozoic being mostly braided [151–153] and shifting to include meandering patterns from late Silurian times onwards when the evolution of rooted vegetation began to stabilise riverbanks and slopes [30,150].

A coal layer in channel sandstone unit 2 (Figure 5d), which is deposited on top of a localised paleosol containing abundant rock fragments, in situ plant rootlets and plant debris,

further suggests a densely vegetated paleoenvironment in a warm climate. Mudcracks a little higher in the succession indicate intermittent periods of drying and aridity (Figure 5f). The presence of fusain (paleo-charcoal) suggests that ancient wildfires affected this region during the Viséan. The examples from Donegal described by Nichols and Jones [21] and Graham [67] occur at various stratigraphies broadly of Viséan age, and represent substantial, recurring burning events. Large paleo-fires were likely fuelled by dry periods, abundant vegetation and an increased amount of atmospheric oxygen during the Carboniferous [81,154,155]. Events such as these profoundly influence denudation rates, resulting in a very large amount of sediment being produced and remobilized [20,23,26,27,147,156]. Once vegetation cover is removed, slope failure and mass wasting become common, flushing even more detritus into the sedimentary system and likely increasing flow energy and sediment load, resulting in highly erosive bases and the introduction of a higher degree of provenance variability within the channelised units.

Presently, in the Himalayas, the parts of the orogenic belt that are impacted by monsoons yield the highest amount of sediment, even compared to high-altitude slopes [157–160]. A study from the South China Sea also revealed more intense erosion rates driven by monsoon activity [161]. This indicates that monsoonal effects have the capacity to directly influence erosion rates. Many modern studies, e.g., [161–164], further support this. It is suggested here that a complex interplay between ambient semi-arid paleoclimatic conditions (fluctuating between wet monsoonal phases, interspersed between much dryer and more arid intervals), the establishment of plant life in and around the MSFm fluvial system, and the enhanced propensity for initiation of wildfires all played a significant role in sediment erosion and transport. These factors can explain the large variability in the detrital sediment signatures observed throughout a relatively short period during the Arundian regional substage (Figure 10). The MSFm being a relatively small-medium scale drainage basin with quite rapid rates of deposition further enhances this already variable detrital signature. The lack of homogenisation in small-scale systems more readily preserves variable provenance signatures, which would likely be diluted and well-mixed in larger and more well-developed fluvial systems, homogenising provenance signatures.

4.4. Final Considerations: Biases in Provenance Analysis

In addition to the inherent differences in grain composition, chemistry and behaviour, there are also mineral fertility differences within source rocks. The Grenville Orogeny is known to have relatively high zircon fertility [143,165], and Caledonian-aged source terranes are relatively low in zircon [119,143,165–167]. These two factors combined offer an explanation for why there are relatively few Caledonian-aged zircon grains in the Bunatrahir West Mullaghmore Sandstone Formation (MSFm) data, and also for the lack of apatite grains yielding Grenville ages.

A source identified in the apatite data (1.6–1.5 Ga I-type/mafic igneous apatite) for unit 1 appears to be completely absent in the zircon data for the same unit (see Figure 8), likely due to low fertility of zircon in the source rock because of its mafic nature [16]. The ability to recognise zircon-poor sources (such as mafic rocks) is powerful and can be done by integrating U-Pb zircon with combined apatite and apatite trace element analysis. This bespoke multi-proxy approach can thus help identify recycled populations (Anders et al. [48] reported similar findings from MSFm sections in County Sligo and County Donegal). The meta-sedimentary rocks of the Neoproterozoic Dalradian Supergroup were one of the sediment sources for the MSFm. The Dalradian metasediments were originally deposited on the southern margin of Laurentia and sourced from the ancient Laurentian continent [138,168]. Remnants of the 'original' Paleoproterozoic to Mesoproterozoic sources that delivered detritus to the Dalradian Supergroup, such as Rockall, Porcupine, Stanton Banks, and Annagh Gneiss Complex, are also likely to be the 'primary' source for detrital zircon grains in the MSFm. Some of the Paleoproterozoic to Mesoproterozoic zircon (and apatite) population thus must be recycled. K-feldspars are likely not sourced from the Dalradian Supergroup, as they are first cycle grains [169]; furthermore the Neoproterozoic succession is composed

of feldspar-poor pelites and psammites, which cannot be a source for the large > 10 mm K-feldspar grains found in the MSFm. The Dalradian Supergroup was a significant source for sandstones only in units 2 and 5. By default, some Paleoproterozoic to Mesoproterozoic zircon grains must be recycled in these units and an elevated number of grains from this time interval should be expected in the zircon data for these units (representing 'original' sourcing + recycled detritus). The provenance signals are, however, so variable in each unit that this trend is not evident. Temporal variations in sediment supply overshadow recycling signatures in this estuarine/fluvial system.

5. Conclusions

This study highlights temporal fluctuations in sediment supply to the Northwest Carboniferous Basin—a medium-scale Viséan basin with a fluvio/estuarine fill sequence represented by the Mullaghmore Sandstone Formation. While it remains difficult to unequivocally identify the precise causes for switching on and off from particular sources, variable detrital sediment composition and fluctuating relative abundance of various source terranes, the bespoke multi-sampling multi-proxy provenance approach adopted here aids in deciphering the complex sedimentological history of the Northwest Carboniferous Basin. Offshore Ireland and Scotland Paleoproterozoic to Mesoproterozoic sources (such as the Rockall and Porcupine banks, the Rhinns Complex and the Annagh Gneiss Complex) are dominant in all samples from the Mullaghmore Sandstone Formation (MSFm), across all proxies. Archean zircons increase in age through the c. 52 m succession of MSFm exposed at Bunatrahir West, and less radiogenic K-feldspar grains become more prominent with the development of this fluvial system, likely representing channel evolution and catchment expansion, where the fluvial system taps farther and deeper into its hinterland. Caledonian-aged detritus and Dalradian Supergroup sediments are variable in all samples and as these are both the most proximal and youngest source terranes, channel avulsion/migration or regional un-roofing are the likely cause of this trend. It is also probable that seasonal climate fluctuations (oscillating between wet monsoons and dry/arid intervals) coupled with contemporary wildfire activity led to modification of vegetation cover and exacerbated bank and hinterland instability, leading to further enhancement of this fluctuating sand supply.

Every basin and every sedimentary sequence is unique and requires thorough investigation of the type of system, scale, paleogeographic and climatic history, and any regional events that may have influenced the system. Consistent provenance sources (with limited fluctuations) have previously been reported for the Carboniferous turbiditic to deltaic infill sequence of the Carboniferous Shannon Basin (located farther south from the NWCB in Ireland; see Nauton-Fourteu et al. [170] and the Jurassic-aged Blackhawk–Castlegate fluvio-deltaic-marine succession in Utah, United States [171]. Both of these sedimentary successions were more mature and homogenised in comparison to the MSFm, indicating that basin scale and physiography are key factors to consider. In the case of the MSFm, the more modest-scale fluvial/estuarine sequence it represents shows highly variable sediment delivery through time within paleo-channels, most likely caused by a mix of monsoonal climate, paleo-wildfires, catchment expansion and channel migration/avulsion. These variations were likely amplified by relatively rapid sediment deposition and a lack of homogenisation.

Finally, combined U-Pb geochronology and trace elements in apatite (in addition to zircon and feldspar proxies) allows for the identification of sources that U-Pb zircon geochronology does not detect, such as mafic terranes and magma-poor metamorphic orogenic belts.

Supplementary Materials: The following supporting information can be downloaded at: https://www.mdpi.com/article/10.3390/geosciences12010020/s1, Figure S1: Single plots for Pb-in-K-feldspar data; Figure S2: Caledonian U-Pb apatite geochronology and trace elements; Table S1: Pb-in-K-feldpsar isotopic data; Table S2: Apatite U-Pb geochronology; Table S3: Zircon U-Pb geochronology;

Table S4: Apatite trace elements; Table S5: Trace elements in apatite SVM prediction with age; Table S6: Petrographic analysis.

Author Contributions: B.A., conceptualization (Lead), data curation (Lead), formal analysis (Lead), investigation (Lead), methodology (Lead), funding acquisition (Lead) writing—original draft (Lead); S.T., conceptualization (Equal), funding acquisition (Equal), investigation (Equal), methodology (Equal), project administration (Lead), supervision (Lead), writing—review and editing (Equal); D.C., formal analysis (Supporting), data curation (Supporting), writing—review and editing (Supporting); J.M., writing—review and editing (Supporting); C.M., formal analysis (Supporting), writing—review and editing (Supporting); G.O., data curation (Supporting), writing—review and editing (Supporting); J.G., investigation (Supporting); E.B., formal analysis (Supporting). All authors have read and agreed to the published version of the manuscript.

Funding: Funding for this research was obtained by the Hardiman Scholarship of NUI, Galway, CASP fieldwork grant, Thomas Crawford Hayes and IAS postgraduate Grants. S.T., D.C., J.M. and E.B. are partly or fully supported by research grants from Science Foundation Ireland (SFI) under Grant Number 13/RC/2092 (iCRAG), which is co-funded under the European Regional Development Fund and by PIPCO RSG. This grant also supported the purchase of the Teledyne Cetac G2 laser ablation system at NCIG, used in this study. C.M. is funded by grant no. 18/SIRG/5559 from Science Foundation Ireland. The National Centre for Isotope Geochemistry (NCIG) was funded primarily by Science Foundation Ireland including grants 04/BR/ES0007/EC07 and 04/BR/ES0007S1 awarded to J.S. Daly.

Data Availability Statement: Supplementary data can be found attached as Excel file.

Acknowledgments: Special thanks to C. Reid and L. O'Connor (iCRAGlabs@TCD) and J. S. Daly (National Centre for Isotope Geochemistry, UCD) for technical assistance. Three anonymous referees and associate editor Sorin Hadrian Petrescu are acknowledged for their helpful comments, which improved this paper.

Conflicts of Interest: The authors declare no conflict of interest.

References

1. Bauer, B.O.; Bull, W.B. Geomorphic Responses to Climatic Change. *Geogr. Rev.* **1993**, *83*, 114. [CrossRef]
2. Leeder, M.R.; Harris, T.; Kirkby, M. Sediment supply and climate change: Implications for basin stratigraphy. *Basin Res.* **1998**, *10*, 7–18. [CrossRef]
3. Sun, J.; Zhu, X. Temporal variations in Pb isotopes and trace element concentrations within Chinese eolian deposits during the past 8Ma: Implications for provenance change. *Earth Planet. Sci. Lett.* **2010**, *290*, 438–447. [CrossRef]
4. McKIE, T. Climatic and Tectonic Controls on Triassic Dryland Terminal Fluvial System Architecture, Central North Sea. *Inter. Associat. Sedimentol. Spec. Pub.* **2014**, *46*, 19–57.
5. Koss, F.G.E.J.E. An Experimental Study of the Effects of Base-Level Change on Fluvial, Coastal Plain and Shelf Systems. *J. Sediment. Res.* **1994**, *64*, 90–98. [CrossRef]
6. Blum, M.D.; Törnqvist, T.E. Fluvial responses to climate and sea-level change: A review and look forward. *Sedimentology* **2000**, *47*, 2–48. [CrossRef]
7. Ericson, J.P.; Vorosmarty, C.; Dingman, S.L.; Ward, L.G.; Meybeck, M. Effective sea-level rise and deltas: Causes of change and human dimension implications. *Glob. Planet. Chang.* **2006**, *50*, 63–82. [CrossRef]
8. Chakrapani, G. Factors controlling variations in river sediment loads. *Curr. Sci.* **2005**, *88*, 569–575.
9. Moreno, C.J.; Horton, B.K.; Caballero, V.; Mora, A.; Parra, M.; Sierra, J. Depositional and provenance record of the Paleogene transition from foreland to hinterland basin evolution during Andean orogenesis, northern Middle Magdalena Valley Basin, Colombia. *J. S. Am. Earth Sci.* **2011**, *32*, 246–263. [CrossRef]
10. Olivarius, M.; Rasmussen, E.S.; Siersma, V.; Knudsen, C.; Kokfelt, T.F.; Keulen, N. Provenance signal variations caused by facies and tectonics: Zircon age and heavy mineral evidence from Miocene sand in the north-eastern North Sea Basin. *Mar. Pet. Geol.* **2014**, *49*, 1–14. [CrossRef]
11. Castelltort, S.; Driessche, J.V.D. How plausible are high-frequency sediment supply-driven cycles in the stratigraphic record? *Sediment. Geol.* **2003**, *157*, 3–13. [CrossRef]
12. Clift, P.D.; Hodges, K.; Heslop, D.; Hannigan, R.; Van Long, H.; Calvès, G. Correlation of Himalayan exhumation rates and Asian monsoon intensity. *Nat. Geosci.* **2008**, *1*, 875–880. [CrossRef]
13. Ashmore, P. Channel Morphology and Bed Load Pulses in Braided, Gravel-Bed Streams. *Geogr. Ann. Ser. A Phys. Geogr.* **1991**, *73*, 37–52. [CrossRef]

14. Repasch, M.; Karlstrom, K.; Heizler, M.; Pecha, M. Birth, and evolution of the Rio Grande fluvial system in the past 8 Ma: Progressive downward integration and the influence of tectonics, volcanism, and climate. *Earth Sci. Rev.* **2017**, *168*, 113–164. [CrossRef]
15. DeCelles, P.G. Lithologic provenance modeling applied to the Late Cretaceous synorogenic Echo Canyon Con-glomerate, Utah: A case of multiple source areas. *Geology* **1988**, *16*, 1039–1043. [CrossRef]
16. Spiegel, C.; Siebel, W.; Kuhlemann, J.; Frisch, W. *Toward a Comprehensive Provenance Analysis: A Multi-Method Approach and Its Implications for the Evolution of the Central Alps*; Geological Society of America: Boulder, CO, USA, 2004.
17. Hovius, N.; Stark, C.; Hao-Tsu, C.; Jiun-Chuan, L. Supply and Removal of Sediment in a Landslide-Dominated Mountain Belt: Central Range, Taiwan. *J. Geol.* **2000**, *108*, 73–89. [CrossRef]
18. Korup, O. Large landslides and their effect on sediment flux in South Westland, New Zealand. *Earth Surf. Process. Landf.* **2005**, *30*, 305–323. [CrossRef]
19. Milliman, J.D.; Kao, S. Hyperpycnal Discharge of Fluvial Sediment to the Ocean: Impact of Super-Typhoon Herb (1996) on Taiwanese Rivers. *J. Geol.* **2005**, *113*, 503–516. [CrossRef]
20. Florsheim, J.; Keller, E.A.; Best, D.W. Fluvial sediment transport in response to moderate storm flows following chaparral wildfire, Ventura County, southern California. *GSA Bull.* **1991**, *103*, 504–511. [CrossRef]
21. Nichols, G.; Jones, T. Fusain in Carboniferous shallow marine sediments, Donegal, Ireland: The sedimentological effects of wildfire. *Sedimentology* **1992**, *39*, 487–502. [CrossRef]
22. Falcon-Lang, H. Fire ecology of the Carboniferous tropical zone. *Palaeogeogr. Palaeoclim. Palaeoecol.* **2000**, *164*, 339–355. [CrossRef]
23. Legleiter, C.J.; Lawrence, R.L.; Fonstad, M.; Marcus, W.A.; Aspinall, R. Fluvial response a decade after wildfire in the northern Yellowstone ecosystem: A spatially explicit analysis. *Geomorphology* **2003**, *54*, 119–136. [CrossRef]
24. Lane, P.N.; Sheridan, G.J.; Noske, P.J. Changes in sediment loads and discharge from small mountain catchments following wildfire in southeastern Australia. *J. Hydrol.* **2006**, *331*, 495–510. [CrossRef]
25. Warrick, J.A.; Rubin, D.M. Suspended-sediment rating curve response to urbanization and wildfire, Santa Ana River, California. *J. Geophys. Res. Earth Surf.* **2007**, *112*, F02018. [CrossRef]
26. Silins, U.; Stone, M.; Emelko, M.B.; Bladon, K. Sediment production following severe wildfire and post-fire salvage logging in the Rocky Mountain headwaters of the Oldman River Basin, Alberta. *Catena* **2009**, *79*, 189–197. [CrossRef]
27. Warrick, J.A.; Hatten, J.A.; Pasternack, G.; Gray, A.; Goni, M.; Wheatcroft, R.A. The effects of wildfire on the sediment yield of a coastal California watershed. *GSA Bull.* **2012**, *124*, 1130–1146. [CrossRef]
28. Operstein, V.; Frydman, S. The Influence of Vegetation on Soil Strength. *Proceed. Institut. Civil Eng.-Ground Improv.* **2000**, *4*, 81–89. [CrossRef]
29. Wiel, M.J.V.D.; Darby, S.E. A new model to analyse the impact of woody riparian vegetation on the ge-otechnical stability of riverbanks. Earth Surface Processes and Landforms. *J. Br. Geomorphol. Res. Group* **2007**, *32*, 2185–2198.
30. Schumm, S.A. Speculations Concerning Paleohydrologic Controls of Terrestrial Sedimentation. *GSA Bull.* **1968**, *79*, 1573. [CrossRef]
31. Osterkamp, W.R.; Hupp, C.R. Fluvial processes and vegetation-glimpses of the past, the present, and perhaps the future. *Geomorphology* **2010**, *116*, 274–285. [CrossRef]
32. Hunsinger, G.B.; Mitra, S.; Warrick, J.A.; Alexander, C.R. Oceanic loading of wildfire-derived organic compounds from a small mountainous river. *J. Geophys. Res. Space Phys.* **2008**, *113*. [CrossRef]
33. Dearing, J.; Jones, R.T. Coupling temporal and spatial dimensions of global sediment flux through lake and marine sediment records. *Glob. Planet. Chang.* **2003**, *39*, 147–168. [CrossRef]
34. Morehead, M.D.; Syvitski, J.P.; Hutton, E.; Peckham, S. Modeling the temporal variability in the flux of sediment from ungauged river basins. *Glob. Planet. Chang.* **2003**, *39*, 95–110. [CrossRef]
35. Douglas, I. The Efficiency of Humid Tropical Denudation Systems. *Trans. Inst. Br. Geogr.* **1969**, 1–16. [CrossRef]
36. Saunders, I.; Young, A. Rates of surface processes on slopes, slope retreat and denudation. *Earth Surf. Process. Landf.* **1983**, *8*, 473–501. [CrossRef]
37. Allen, J.P.; Fielding, C.R.; Gibling, M.R.; Rygel, M. Fluvial response to paleo-equatorial climate fluctuations during the late Paleozoic ice age. *GSA Bull.* **2011**, *123*, 1524–1538. [CrossRef]
38. Fielding, C.R.; Allen, J.P.; Alexander, J.; Gibling, M.R. Facies model for fluvial systems in the seasonal tropics and subtropics. *Geology* **2009**, *37*, 623–626. [CrossRef]
39. Welland, M. *Sand: The Never-Ending Story*; University of California Press: Oakland, CA, USA, 2009.
40. Yang, S.-L.; Zhao, Q.-Y.; Belkin, I.M. Temporal variation in the sediment load of the Yangtze River and the influences of human activities. *J. Hydrol.* **2002**, *263*, 56–71. [CrossRef]
41. Gregory, K. The human role in changing river channels. *Geomorphology* **2006**, *79*, 172–191. [CrossRef]
42. Zheng, M.; Qin, F.; Yang, J.; Cai, Q. The spatio-temporal invariability of sediment concentration and the flow–sediment relationship for hilly areas of the Chinese Loess Plateau. *Catena* **2013**, *109*, 164–176. [CrossRef]
43. Peng, J.; Chen, S.; Dong, P. Temporal variation of sediment load in the Yellow River basin, China, and its impacts on the lower reaches and the river delta. *Catena* **2010**, *83*, 135–147. [CrossRef]
44. Chalov, S.R.; Jarsjö, J.; Kasimov, N.S.; Romanchenko, A.O.; Pietro, J.; Thorslund, J.; Promakhova, E.V. Spa-tio-temporal variation of sediment transport in the Selenga River Basin, Mongolia, and Russia. *Environ. Earth Sci.* **2015**, *73*, 663–680. [CrossRef]

45. Kwon, Y.-I.; Boggs, S.; Jr, S.B. Provenance interpretation of Tertiary sandstones from the Cheju Basin (NE East China Sea): A comparison of conventional petrographic and scanning cathodoluminescence techniques. *Sediment. Geol.* **2002**, *152*, 29–43. [CrossRef]
46. Franklin, J.; Tyrrell, S.; Morton, A.; Frei, D.; Mark, C. Triassic sand supply to the Slyne Basin, offshore western Ireland—New insights from a multi-proxy provenance approach. *J. Geol. Soc.* **2019**, *176*, 1120–1135. [CrossRef]
47. Hietpas, J.; Samson, S.; Moecher, D.; Chakraborty, S. Enhancing tectonic and provenance information from detrital zircon studies: Assessing terrane-scale sampling and grain-scale characterization. *J. Geol. Soc.* **2011**, *168*, 309–318. [CrossRef]
48. Anders, B.; Tyrrell, S.; Chew, D.; Mark, C.; O'Sullivan, G.; Murray, J.; Graham, J.; Badenszki, E. Spatial variation in provenance signal: Identifying complex sand sourcing within a Carboniferous basin using multiproxy provenance analysis. *J. Geol. Soc.* **2021**, *179*, jgs2021-045. [CrossRef]
49. Graham, J.R. The carboniferous geology of north mayo. *Ir. J. Earth Sci.* **2010**, *28*, 25–45. [CrossRef]
50. Scotese, C.; McKerrow, W.S. Revised World maps and introduction. *Geol. Soc. Lond. Mem.* **1990**, *12*, 1–21. [CrossRef]
51. Blakey, R.C.; Fielding, C.R.; Frank, T.D.; Isbell, J.L. Gondwana paleogeography from assembly to breakup—A 500 m.y. odyssey. *Geol. Soc. Am. Spec. Pap.* **2008**, *441*, 1–28. [CrossRef]
52. Barham, M.; Murray, J.; Joachimski, M.M.; Williams, D.M. The onset of the Permo-Carboniferous glaciation: Reconciling global stratigraphic evidence with biogenic apatite δ18O records in the late Visean. *J. Geol. Soc.* **2012**, *169*, 119–122. [CrossRef]
53. Leeder, M. Tectonic and palaeogeographic models for Lower Carboniferous Europe. *Geol. J. Spec. Issue* **1987**, *12*, 1–20.
54. Pulham, A.J. Controls on internal structure and architecture of sandstone bodies within Upper Carboniferous fluvial-dominated deltas, County Clare, western Ireland. *Geol. Soc. Lond. Spéc. Publ.* **1989**, *41*, 179–203. [CrossRef]
55. Nauton-Fourteu, M.; Tyrrell, S.; Chew, D.M.; Drakou, F.; Pfaff, K.; Jobe, Z. Deep-versus shallow-marine sandstone provenance in the mid-Carboniferous Clare Basin, western Ireland. *J. Geol. Soc.* **2021**, *178*, jgs2020-216. [CrossRef]
56. Clayton, G.; Higgs, K. The Tournaisian marine transgression in Ireland. *J. Earth Sci.* **1979**, *2*, 1–10.
57. Clayton, G.; Graham, J.R.; Higgs, K.T.; Sevastopulo, G.D.; Welsh, A. Late Devonian and Early Carboniferous palaeogeography of southern Ireland and southwest Britain. *Ann. Société Géologique Belg.* **1986**, *109*, 103–111.
58. Graham, J.R.; Sevastopulo, G.D. The stratigraphy of latest Devonian and earliest Carboniferous rocks in Ireland. *Palaeobiodiversity Palaeoenvironments* **2020**, *101*, 515–527. [CrossRef]
59. Worthington, R.P.; Walsh, J.J. Structure of Lower Carboniferous basins of NW Ireland, and its implications for structural inheritance and Cenozoic faulting. *J. Struct. Geol.* **2011**, *33*, 1285–1299. [CrossRef]
60. Leeder, M.R. Upper Palaeozoic basins of the British Isles—Caledonide inheritance versus Hercynian plate margin processes. *J. Geol. Soc.* **1982**, *139*, 479–491. [CrossRef]
61. Sevastopulo, G.D.; Wyse Jackson, P.N. Carboniferous: Mississippian (Tournaisian and Viséan). In *The Geology of Ireland*; Holland, C., Sanders, I., Eds.; Dunedin Academic Press Ltd.: Edinburgh, UK, 2009.
62. Philcox, M.E.; Baily, H.; Clayton, G.; Sevastopulo, G.D. Evolution of the Carboniferous Lough Allen Basin, Northwest Ireland. *Geol. Soc. Lond. Spéc. Publ.* **1992**, *62*, 203–215. [CrossRef]
63. Somerville, I.D.; Cózar, P.; Aretz, M.; Herbig, H.-G.; Mitchell, W.I.; Medina-Varea, P. Carbonate facies and biostromal distribution in a tectonically controlled platform in northwest Ireland during the late Viséan (Mississippian). *Proc. Yorks. Geol. Soc.* **2009**, *57*, 165–192. [CrossRef]
64. Graham, J.R. The Mullaghmore Sandstone Formation of north-west Ireland: A regional Mississippian lowstand deposit. *Ir. J. Earth Sci.* **2017**, *35*, 19. [CrossRef]
65. George, T.N.; Oswald, D.H. The Carboniferous rocks of the Donegal syncline. *Q. J. Geol. Soc.* **1957**, *113*, 137–183. [CrossRef]
66. Hubbard, J.A.E.B. Facies Patterns in the Carrowmoran Sandstone (Visean) of Western Co. Sligo, Ireland. *Proc. Geol. Assoc.* **1966**, *77*, 233–254. [CrossRef]
67. Graham, J.R. Dinantian river systems and coastal zone sedimentation in northwest Ireland. *Geol. Soc. Lond. Spéc. Publ.* **1996**, *107*, 183–206. [CrossRef]
68. Connolly, N. Sedimentology Analysis and Correlation of the Mullaghmore Sandstone Formation in the North and Northwest of Ireland. PhD Thesis, Trinity College Dublin, Dublin, Ireland, 2003.
69. Ketzer, J.M.; Morad, S.; Evans, R.; Al-Aasm, I. Distribution of Diagenetic Alterations in Fluvial, Deltaic, and Shallow Marine Sandstones within a Sequence Stratigraphic Framework: Evidence from the Mullaghmore Formation (Carboniferous), NW Ireland. *J. Sediment. Res.* **2002**, *72*, 760–774. [CrossRef]
70. Higgs, K. Stratigraphic Palynology of the Carboniferous Rocks in Northwest Ireland. *Bull. Geol. Surv. Irel.* **1984**, *3*, 171–202.
71. Clayton, G. Dinantian miospores and intercontinental correlation. *Congrès Int. Stratigr. Géologie Carbonifère* **1985**, *10*, 9–23.
72. Poty, E.; Devuyst, F.-X.; Hance, L. Upper Devonian, and Mississippian foraminiferal and rugose coral zonations of Belgium and northern France: A tool for Eurasian correlations. *Geol. Mag.* **2006**, *143*, 829–857. [CrossRef]
73. Wright, V.P. Equatorial aridity and climatic oscillations during the early Carboniferous, southern Britain. *J. Geol. Soc.* **1990**, *147*, 359–363. [CrossRef]
74. Wright, V.P.; Vanstone, S.D. Onset of Late Palaeozoic glacio-eustasy and the evolving climates of low latitude areas: A synthesis of current understanding. *J. Geol. Soc.* **2001**, *158*, 579–582. [CrossRef]
75. Falcon-Lang, H.J. The Early Carboniferous (Courceyan—Arundian) monsoonal climate of the British Isles: Evidence from growth rings in fossil woods. *Geol. Mag.* **1999**, *136*, 177–187. [CrossRef]

76. Davies, S.J.; Fielding, C. The record of Carboniferous sea-level change in low-latitude sedimentary successions from Britain and Ireland during the onset of the late Paleozoic ice age Resolving the Late Paleozoic Ice Age in Time and Space. *Geol. Soc. Am. Boulder* **2008**, *441*, 187–204.
77. Fielding, C.R.; Frank, T.D.; Isbell, J.L. *The Late Paleozoic Ice Age-A Review of Current Understanding and Synthesis of Global Climate Patterns Resolving the Late Paleozoic Ice Age in Time and Space*; Geological Society of America: Boulder, CO, USA, 2008; pp. 343–354.
78. Montañez, I.P.; Poulsen, C.J. The Late Paleozoic Ice Age: An Evolving Paradigm. *Annu. Rev. Earth Planet. Sci.* **2013**, *41*, 629–656. [CrossRef]
79. Collinson, M.E.; Scott, A.C. Implications of vegetational change through the geological record on models for coal-forming environments. *Geol. Soc. Lond. Spéc. Publ.* **1987**, *32*, 67–85. [CrossRef]
80. Falcon-Lang, H. The impact of wildfire on an Early Carboniferous coastal environment, North Mayo, Ireland. *Palaeogeogr. Palaeoclim. Palaeoecol.* **1998**, *139*, 121–138. [CrossRef]
81. Berner, R.A.; Canfield, D. A new model for atmospheric oxygen over Phanerozoic time. *Am. J. Sci.* **1989**, *289*, 333–361. [CrossRef]
82. Berner, R.A.; Beerling, D.J.; Dudley, R.; Robinson, J.M.; Wildman, R.A., Jr. Phanerozoic atmospheric oxygen. *Annu. Rev. Earth Planet. Sci.* **2003**, *31*, 105–134. [CrossRef]
83. Berner, R.A. Phanerozoic atmospheric oxygen: New results using the GEOCARBSULF model. *Am. J. Sci.* **2009**, *309*, 603–606. [CrossRef]
84. Tyrrell, S.; Haughton, P.D.; Daly, J.S.; Shannon, P.M.; Sylvester, P. The Pb isotopic composition of detrital K-feldspar: A tool for constraining provenance, sedimentary processes and paleodrainage. *Quant. Mineral. Microanal. Sediments Sediment. Rocks. Mineral. Assoc. Can. Short Course Ser.* **2012**, *42*, 203–217.
85. Souders, A.K.; Sylvester, P.J. Accuracy, and precision of non-matrix-matched calibration for lead isotope ratio measurements of lead-poor minerals by LA-MC-ICPMS. *J. Anal. At. Spectrom.* **2010**, *25*, 975–988. [CrossRef]
86. Thomson, S.N.; Gehrels, G.E.; Ruiz, J.; Buchwaldt, R. Routine low-damage apatite U-Pb dating using laser ablation-multicollector-ICPMS. *Geochem. Geophys. Geosyst.* **2012**, *13*. [CrossRef]
87. McDowell, F.W.; McIntosh, W.C.; Farley, K. A precise 40Ar–39Ar reference age for the Durango apatite (U–Th)/He and fission-track dating standard. *Chem. Geol.* **2005**, *214*, 249–263. [CrossRef]
88. Schoene, B.; Bowring, S.A. U–Pb systematics of the McClure Mountain syenite: Thermochronological constraints on the age of the 40Ar/39Ar standard MMhb. *Contrib. Miner. Pet.* **2006**, *151*, 615–630. [CrossRef]
89. Wiedenbeck, M.A.P.C.; Alle, P.; Corfu, F.Y.; Griffin, W.L.; Meier, M.; Oberli, F.V.; von Quadt, A.; Roddick, J.C.; Spiegel, W. Three Natural Zircon Standards for U-Th-Pb, Lu-Hf, Trace Element and Ree Analyses. *Geostand. Newsl.* **1995**, *19*, 1–23. [CrossRef]
90. Sláma, J.; Košler, J.; Condon, D.; Crowley, J.; Gerdes, A.; Hanchar, J.M.; Horstwood, M.; Morris, G.A.; Nasdala, L.; Norberg, N.; et al. Plešovice zircon—A new natural reference material for U–Pb and Hf isotopic microanalysis. *Chem. Geol.* **2008**, *249*, 1–35. [CrossRef]
91. Pointon, M.A.; Cliff, R.A.; Chew, D.M. The provenance of Western Irish Namurian Basin sedimentary strata inferred using detrital zircon U-Pb LA-ICP-MS geochronology. *Geol. J.* **2011**, *47*, 77–98. [CrossRef]
92. Paton, C.; Hellstrom, J.; Paul, B.; Woodhead, J.; Hergt, J. Iolite: Freeware for the visualization and processing of mass spectrometric data. *J. Anal. At. Spectrom.* **2011**, *26*, 2508–2518. [CrossRef]
93. Chew, D.; Petrus, J.; Kamber, B. U–Pb LA–ICPMS dating using accessory mineral standards with variable common Pb. *Chem. Geol.* **2014**, *363*, 185–199. [CrossRef]
94. Petrus, J.A.; Kamber, B. VizualAge: A Novel Approach to Laser Ablation ICP-MS U-Pb Geochronology Data Reduction. *Geostand. Geoanal. Res.* **2012**, *36*, 247–270. [CrossRef]
95. Ludwig, K. *User's Manual for Isoplot Version 3.75–4.15: A Geochronological Toolkit for Microsoft Excel. 5*; Berkley Geochronological Centre: Berkeley, CA, USA, 2012.
96. Chew, D.M.; Sylvester, P.J.; Tubrett, M.N. U–Pb and Th–Pb dating of apatite by LA-ICPMS. *Chem. Geol.* **2011**, *280*, 200–216. [CrossRef]
97. Stacey, J.S.; Kramers, J.D. Approximation of terrestrial lead isotope evolution by a two-stage model. *Earth Planet. Sci. Lett.* **1975**, *26*, 207–221. [CrossRef]
98. Mark, C.; Cogné, N.; Chew, D. Tracking exhumation and drainage divide migration of the Western Alps: A test of the apatite U-Pb thermochronometer as a detrital provenance tool. *GSA Bull.* **2016**, *128*, 1439–1460. [CrossRef]
99. Vermeesch, P.; Resentini, A.; Garzanti, E. An R package for statistical provenance analysis. *Sediment. Geol.* **2016**, *336*, 14–25. [CrossRef]
100. Chew, D.M.; Babechuk, M.G.; Cogné, N.; Mark, C.; O'Sullivan, G.; Henrichs, I.A.; Doepke, D.; McKenna, C.A. (LA,Q)-ICPMS trace-element analyses of Durango and McClure Mountain apatite and implications for making natural LA-ICPMS mineral standards. *Chem. Geol.* **2016**, *435*, 35–48. [CrossRef]
101. Woodhead, J.D.; Hellstrom, J.; Hergt, J.M.; Greig, A.; Maaß, R. Isotopic and Elemental Imaging of Geological Materials by Laser Ablation Inductively Coupled Plasma-Mass Spectrometry. *Geostand. Geoanalytical Res.* **2007**, *31*, 331–343. [CrossRef]
102. O'Sullivan, G.; Chew, D.; Kenny, G.; Henrichs, I.; Mulligan, D. The trace element composition of apatite and its application to detrital provenance studies. *Earth Sci. Rev.* **2020**, *201*. [CrossRef]
103. O'Sullivan, G.J.; Chew, D.M.; Morton, A.C.; Mark, C.; Henrichs, I.A. An Integrated Apatite Geochronology and Geochemistry Tool for Sedimentary Provenance Analysis. *Geochem. Geophys. Geosystems* **2018**, *19*, 1309–1326. [CrossRef]

104. Morton, A.C.; Hallsworth, C. Identifying provenance-specific features of detrital heavy mineral assemblages in sandstones. *Sediment. Geol.* **1994**, *90*, 241–256. [CrossRef]
105. Corfu, F.; Hanchar, J.M.; Hoskin, P.W.; Kinny, P. Atlas of Zircon Textures. *Rev. Miner. Geochem.* **2003**, *53*, 469–500. [CrossRef]
106. Finch, R. Structure and Chemistry of Zircon and Zircon-Group Minerals. *Rev. Miner. Geochem.* **2003**, *53*, 1–25. [CrossRef]
107. Dickinson, W.R.; Lawton, T.F.; Gehrels, G.E. Recycling detrital zircons: A case study from the Cretaceous Bisbee Group of southern Arizona. *Geology* **2009**, *37*, 503–506. [CrossRef]
108. Mange, M.A.; Maurer, H. *Heavy Minerals in Colour*; Springer: Berlin/Heidelberg, Germany, 2012.
109. Morton, A.C. Stability of detrital heavy minerals in Tertiary sandstones from the North Sea Basin. *Clay Miner.* **1984**, *19*, 287–308. [CrossRef]
110. Lee, J.K.W.; Williams, I.; Ellis, D.J. Pb, U and Th diffusion in natural zircon. *Nature* **1997**, *390*, 159–162. [CrossRef]
111. Mezger, K.; Krogstad, E.J. Interpretation of discordant U-Pb zircon ages: An evaluation. *J. Metamorph. Geol.* **1997**, *15*, 127–140. [CrossRef]
112. Cochrane, R.; Spikings, R.A.; Chew, D.; Wotzlaw, J.-F.; Chiaradia, M.; Tyrrell, S.; Schaltegger, U.; van der Lelij, R. High temperature (>350 °C) thermochronology and mechanisms of Pb loss in apatite. *Geochim. Et Cosmochim. Acta* **2014**, *127*, 39–56. [CrossRef]
113. Chew, D.M.; Spikings, R.A. Geochronology and Thermochronology Using Apatite: Time and Temperature, Lower Crust to Surface. *Elements* **2015**, *11*, 189–194. [CrossRef]
114. Henrichs, I.A.; O'Sullivan, G.; Chew, D.M.; Mark, C.; Babechuk, M.G.; McKenna, C.; Emo, R. The trace element and U-Pb systematics of metamorphic apatite. *Chem. Geol.* **2018**, *483*, 218–238. [CrossRef]
115. Harlov, D.E.; Wirth, R.; Förster, H.-J. An experimental study of dissolution–reprecipitation in fluorapatite: Fluid infiltration and the formation of monazite. *Contrib. Miner. Pet.* **2005**, *150*, 268–286. [CrossRef]
116. O'Sullivan, G.; Chew, D.; Samson, S. Detecting magma-poor orogens in the detrital record. *Geology* **2016**, *44*, 871–874. [CrossRef]
117. Pettijohn, F.J.; Potter, P.E.; Siever, R. *Production and Provenance of Sand*; Springer: New York, NY, USA, 1972; pp. 294–326.
118. Morton, A.C.; Taylor, P.N. Geochemical and isotopic constraints on the nature and age of basement rocks from Rockall Bank, NE Atlantic. *J. Geol. Soc.* **1991**, *148*, 631–634. [CrossRef]
119. Kalsbeek, F.; Nutman, A.P. Anatomy of the Early Proterozoic Nagsuggtoqidian orogen, West Greenland, ex-plored by reconnaissance SHRIMP U-Pb zircon dating. *Geology* **1996**, *24*, 515–518. [CrossRef]
120. van Gool, J.A.; Connelly, J.N.; Marker, M.; Mengel, F.C. The Nagsuggtoqidian Orogen of West Greenland: Tec-tonic evolution and regional correlations from a West Greenland perspective. *Can. J. Earth Sci.* **2002**, *39*, 665–686. [CrossRef]
121. Connelly, J.N.; Thrane, K. Rapid determination of Pb isotopes to define Precambrian allochthonous domains: An example from West Greenland. *Geology* **2005**, *33*, 953. [CrossRef]
122. Nutman, A.P.; Kalsbeek, F.; Friend, C.R. The Nagsuggtoqidian orogen in South-East Greenland: Evidence for Paleoproterozoic collision and plate assembly. *Am. J. Sci.* **2008**, *308*, 529–572. [CrossRef]
123. Scanlon, R.; Daly, J.; Whitehouse, M. The c. 1.8 Ga Stanton Banks Terrane, offshore Western Scotland, a large juvenile Palaeoproterozoic crustal block within the accretionary Lewisian complex. *EGS AGU EUG Jt. Assem.* **2003**, 13248.
124. Daly, J.S. Pre-Caledonian history of the Annagh Gneiss Complex North-Western Ireland, and correlation with Laurentia-Baltica. *Ir. J. Earth Sci.* **1996**, *15*, 5–18.
125. Muir, R.J.; Fitches, W.R.; Maltman, A.J. Rhinns complex: A missing link in the Proterozoic basement of the North Atlantic region. *Geology* **1992**, *20*, 1043–1046. [CrossRef]
126. Chew, D.; Tyrrell, S.; Daly, J.S.; Cogné, N.; Sun, K.; Badenszki, E. *The Basement Geology of the Porcupine High—A Key Transatlantic Link between the Caledonides and Appalachians*; Trinity College Dublin: Dublin, Ireland, 2019.
127. Chew, D. Grampian Orogeny. In *The Geology of Ireland*; Holland, C., Sanders, I., Eds.; Dunedin Academic Press: Edinburgh, UK, 2009; pp. 69–93.
128. Archibald, D.B.; Macquarrie, L.M.; Murphy, J.B.; Strachan, R.A.; McFarlane, C.R.; Button, M.; Larson, K.P.; Dunlop, J. The construction of the Donegal composite batholith, Irish Caledonides: Temporal constraints from U-Pb dating of zircon and titanite. *GSA Bull.* **2021**, *133*, 2335–2354. [CrossRef]
129. St-Onge, M.R.; Wodicka, N.; Ijewliw, O. Polymetamorphic Evolution of the Trans-Hudson Orogen, Baffin Island, Canada: Integration of Petrological, Structural and Geochronological Data. *J. Pet.* **2006**, *48*, 271–302. [CrossRef]
130. Garde, A.A.; Hamilton, M.A.; Chadwick, B.; Grocott, J.; McCaffrey, K. The Ketilidian orogen of South Greenland: Geochronology, tectonics, magmatism, and fore-arc accretion during Palaeoproterozoic oblique convergence. *Can. J. Earth Sci.* **2002**, *39*, 765–793. [CrossRef]
131. McAteer, C.A.; Daly, J.S.; Flowerdew, M.J.; Connelly, J.N.; Housh, T.B.; Whitehouse, M.J. Detrital zircon, detrital titanite and igneous clast U–Pb geochronology and basement–cover relationships of the Colonsay Group, SW Scotland: Laurentian provenance and correlation with the Neoproterozoic Dalradian Supergroup. *Precambrian Res.* **2010**, *181*, 21–42. [CrossRef]
132. McLelland, J.; Daly, J.; McLelland, J.M. The Grenville Orogenic Cycle (ca. 1350–1000 Ma): An Adirondack perspective. *Tectonophysics* **1996**, *265*, 1–28. [CrossRef]
133. Cherniak, D.; Watson, E. Pb diffusion in zircon. *Chem. Geol.* **2001**, *172*, 5–24. [CrossRef]
134. Claesson, S.; Vetrin, V.; Bayanova, T.; Downes, H. U-Pb zircon ages from a Devonian carbonatite dyke, Kola peninsula, Russia: A record of geological evolution from the Archaean to the Palaeozoic. *Lithos* **2000**, *51*, 95–108. [CrossRef]

135. Zimmermann, S.; Mark, C.; Chew, D.; Voice, P.J. Maximising data and precision from detrital zircon U-Pb analysis by LA-ICPMS: The use of core-rim ages and the single-analysis concordia age. *Sediment. Geol.* **2018**, *375*, 5–13. [CrossRef]
136. Turlin, F.; Deruy, C.; Eglinger, A.; Vanderhaeghe, O.; André-Mayer, A.-S.; Poujol, M.; Moukhsil, A.; Solgadi, F. A 70 Ma record of suprasolidus conditions in the large, hot, long-duration Grenville Orogen. *Terra Nova* **2018**, *30*, 233–243. [CrossRef]
137. Dewey, J.F. Orogeny can be very short. *Proc. Natl. Acad. Sci. USA* **2005**, *102*, 15286–15293. [CrossRef]
138. Cawood, P.A.; Nemchin, A.A.; Smith, M.; Loewy, S. Source of the Dalradian Supergroup constrained by U–Pb dating of detrital zircon and implications for the East Laurentian margin. *J. Geol. Soc.* **2003**, *160*, 231–246. [CrossRef]
139. Tyrrell, S.; Haughton, P.; Daly, J.S.; Kokfelt, T.F.; Gagnevin, D. The Use of the Common Pb Isotope Composition of Detrital K-Feldspar Grains as a Provenance Tool and Its Application to Upper Carboniferous Paleodrainage, Northern England. *J. Sediment. Res.* **2006**, *76*, 324–345. [CrossRef]
140. Morton, A.C.; Hallsworth, C.R. Processes controlling the composition of heavy mineral assemblages in sandstones. *Sediment. Geol.* **1999**, *124*, 3–29. [CrossRef]
141. Guidry, M.W.; Mackenzie, F.T. Apatite weathering and the Phanerozoic phosphorus cycle. *Geology* **2000**, *28*, 631–634. [CrossRef]
142. Guidry, M.W.; Mackenzie, F.T. Experimental study of igneous and sedimentary apatite dissolution: Control of pH, distance from equilibrium, and temperature on dissolution rates. *Geochim. Cosmochim. Acta* **2003**, *67*, 2949–2963. [CrossRef]
143. Moecher, D.P.; Samson, S.D. Differential zircon fertility of source terranes and natural bias in the detrital zircon record: Implications for sedimentary provenance analysis. *Earth Planet. Sci. Lett.* **2006**, *247*, 252–266. [CrossRef]
144. Johansson, A.; Gee, D.G.; Larionov, A.N.; Ohta, Y.; Tebenkov, A.M. Grenvillian and Caledonian evolution of eastern Svalbard —A tale of two orogenies. *Terra Nova* **2005**, *17*, 317–325. [CrossRef]
145. Max, M.D.; Sonet, J. A Grenville age for pre-Caledonian rocks in NW Co. Mayo, Ireland. *J. Geol. Soc.* **1979**, *136*, 379–382. [CrossRef]
146. Brook, M.; Brewer, M.S.; Powell, D. Grenville events in Moine rocks of the Northern Highlands, Scotland. *J. Geol. Soc.* **1977**, *133*, 489–496. [CrossRef]
147. Benda, L.; Miller, D.; Bigelow, P.; Andras, K. Effects of post-wildfire erosion on channel environments, Boise River, Idaho. *For. Ecol. Manag.* **2003**, *178*, 105–119. [CrossRef]
148. Moody, J.A.; Martin, D.A. Initial hydrologic and geomorphic response following a wildfire in the Colorado Front Range. *Earth Surf. Process. Landf.* **2001**, *26*, 1049–1070. [CrossRef]
149. Garver, J.; Royce, P.; Smick, T. Chromium and nickel in shale of the Taconic foreland; a case study for the provenance of fine-grained sediments with an ultramafic source. *J. Sediment. Res.* **1996**, *66*, 100–106.
150. Davies, N.; Gibling, M.R. The sedimentary record of Carboniferous rivers: Continuing influence of land plant evolution on alluvial processes and Palaeozoic ecosystems. *Earth Sci. Rev.* **2013**, *120*, 40–79. [CrossRef]
151. Cotter, E. *The Evolution of Fluvial Style, with Special Reference to the Central Appalachian Paleozoic*; Canadian Society of Petroleum Geologists: Calgary, Canada, 1978.
152. Murray, A.B.; Paola, C. Modelling the effect of vegetation on channel pattern in bedload rivers. *Earth Surf. Process. Landf.* **2003**, *28*, 131–143. [CrossRef]
153. Davies, N.; Gibling, M.R. Paleozoic vegetation and the Siluro-Devonian rise of fluvial lateral accretion sets. *Geology* **2010**, *38*, 51–54. [CrossRef]
154. Graham, J.B.; Aguilar, N.M.; Dudley, R.; Gans, C. Implications of the late Palaeozoic oxygen pulse for physiology and evolution. *Nature* **1995**, *375*, 117–120. [CrossRef]
155. Beerling, D.; Lake, J.; Berner, R.; Hickey, L.; Taylor, D.; Royer, D. Carbon isotope evidence implying high O2/CO2 ratios in the Permo-Carboniferous atmosphere. *Geochim. Cosmochim. Acta* **2002**, *66*, 3757–3767. [CrossRef]
156. Murphy, B.P.; Czuba, J.; Belmont, P. Post-wildfire sediment cascades: A modeling framework linking debris flow generation and network-scale sediment routing. *Earth Surf. Process. Landf.* **2019**, *44*, 2126–2140. [CrossRef]
157. Garzanti, E.; Vezzoli, G.; Andò, S.; Lavé, J.; Attal, M.; France-Lanord, C.; DeCelles, P. Quantifying sand provenance and erosion (Marsyandi River, Nepal Himalaya). *Earth Planet. Sci. Lett.* **2007**, *258*, 500–515. [CrossRef]
158. Bookhagen, B.; Thiede, R.C.; Strecker, M.R. Late Quaternary intensified monsoon phases control landscape evolution in the northwest Himalaya. *Geology* **2005**, *33*, 149. [CrossRef]
159. Clift, P.D.; Giosan, L.; Blusztajn, J.; Campbell, I.; Allen, C.M.; Pringle, M.; Tabrez, A.R.; Danish, M.; Rabbani, M.; Alizai, A.; et al. Holocene erosion of the Lesser Himalaya triggered by intensified summer monsoon. *Geology* **2008**, *36*, 79–82. [CrossRef]
160. Li, Y.; Clift, P.D.; Böning, P.; Blusztajn, J.; Murray, R.W.; Ireland, T.; Pahnke, K.; Helm, N.C.; Giosan, L. Continuous Holocene input of river sediment to the Indus Submarine Canyon. *Mar. Geol.* **2018**, *406*, 159–176. [CrossRef]
161. Clift, P.D.; Wan, S.; Blusztajn, J. Reconstructing chemical weathering, physical erosion and monsoon intensity since 25Ma in the northern South China Sea: A review of competing proxies. *Earth Sci. Rev.* **2014**, *130*, 86–102. [CrossRef]
162. Bookhagen, B.; Thiede, R.C.; Strecker, M.R. Abnormal monsoon years and their control on erosion and sediment flux in the high, arid northwest Himalaya. *Earth Planet. Sci. Lett.* **2005**, *231*, 131–146. [CrossRef]
163. Colin, C.; Siani, G.; Sicre, M.-A.; Liu, Z. Impact of the East Asian monsoon rainfall changes on the erosion of the Mekong River basin over the past 25,000yr. *Mar. Geol.* **2010**, *271*, 84–92. [CrossRef]

164. Cui, M.; Wang, Z.; Rao, K.N.; Sangode, S.J.; Saito, Y.; Chen, T.; Kulkarni, Y.; Kumar, K.C.V.N.; Demudu, G. A mid- to late-Holocene record of vegetation decline and erosion triggered by monsoon weakening and human adaptations in the south-east Indian Peninsula. *Holocene* **2017**, *27*, 1976–1987. [CrossRef]
165. Dickinson, W.R. Impact of differential zircon fertility of granitoid basement rocks in North America on age populations of detrital zircons and implications for granite petrogenesis. *Earth Planet. Sci. Lett.* **2008**, *275*, 80–92. [CrossRef]
166. Chew, D.; O'Sullivan, G.; Caracciolo, L.; Mark, C.; Tyrrell, S. Sourcing the sand: Accessory mineral fertility, analytical and other biases in detrital U-Pb provenance analysis. *Earth Sci. Rev.* **2020**, *202*, 103093. [CrossRef]
167. Barham, M.; Kirkland, C.L.; Hovikoski, J.; Alsen, P.; Hollis, J.; Tyrrell, S. Reduce or recycle? Revealing source to sink links through integrated zircon–feldspar provenance fingerprinting. *Sedimentology* **2020**, *68*, 531–556. [CrossRef]
168. Johnson, T.E.; Kirkland, C.L.; Reddy, S.M.; Evans, N.J.; McDonald, B.J. The source of Dalradian detritus in the Buchan Block, NE Scotland: Application of new tools to detrital datasets. *J. Geol. Soc.* **2016**, *173*, 773–782. [CrossRef]
169. Johnson, S.P.; Kirkland, C.L.; Evans, N.J.; McDonald, B.J.; Cutten, H.N. The complexity of sediment recycling as revealed by common Pb isotopes in K-feldspar. *Geosci. Front.* **2018**, *9*, 1515–1527. [CrossRef]
170. Nauton-Fourteu, M.; Tyrrell, S.; Morton, A.; Mark, C.; O'Sullivan, G.J.; Chew, D.M. Constraining recycled detritus in quartz-rich sandstones: Insights from a multi-proxy provenance study of the Mid-Carboniferous, Clare Basin, western Ireland. *Basin Res.* **2020**, *33*, 342–363. [CrossRef]
171. Pettit, B.S.; Blum, M.; Pecha, M.; McLean, N.; Bartschi, N.C.; Saylor, J.E.; Saylo, J.E. Detrital-Zircon U-Pb Paleodrainage Reconstruction and Geochronology of the Campanian Blackhawk–Castlegate Succession, Wasatch Plateau and Book Cliffs, Utah, USA. *J. Sediment. Res.* **2019**, *89*, 273–292. [CrossRef]